Shock and Vibration

Vibration Analysis and Control of Time-Varying Systems

Lead Guest Editor: Xiao-ting Rui
Guest Editors: Dieter Bestle, Chuanzeng Zhang, Xuping Zhang, Pierangelo Masarati, and Chengzhi Yuan

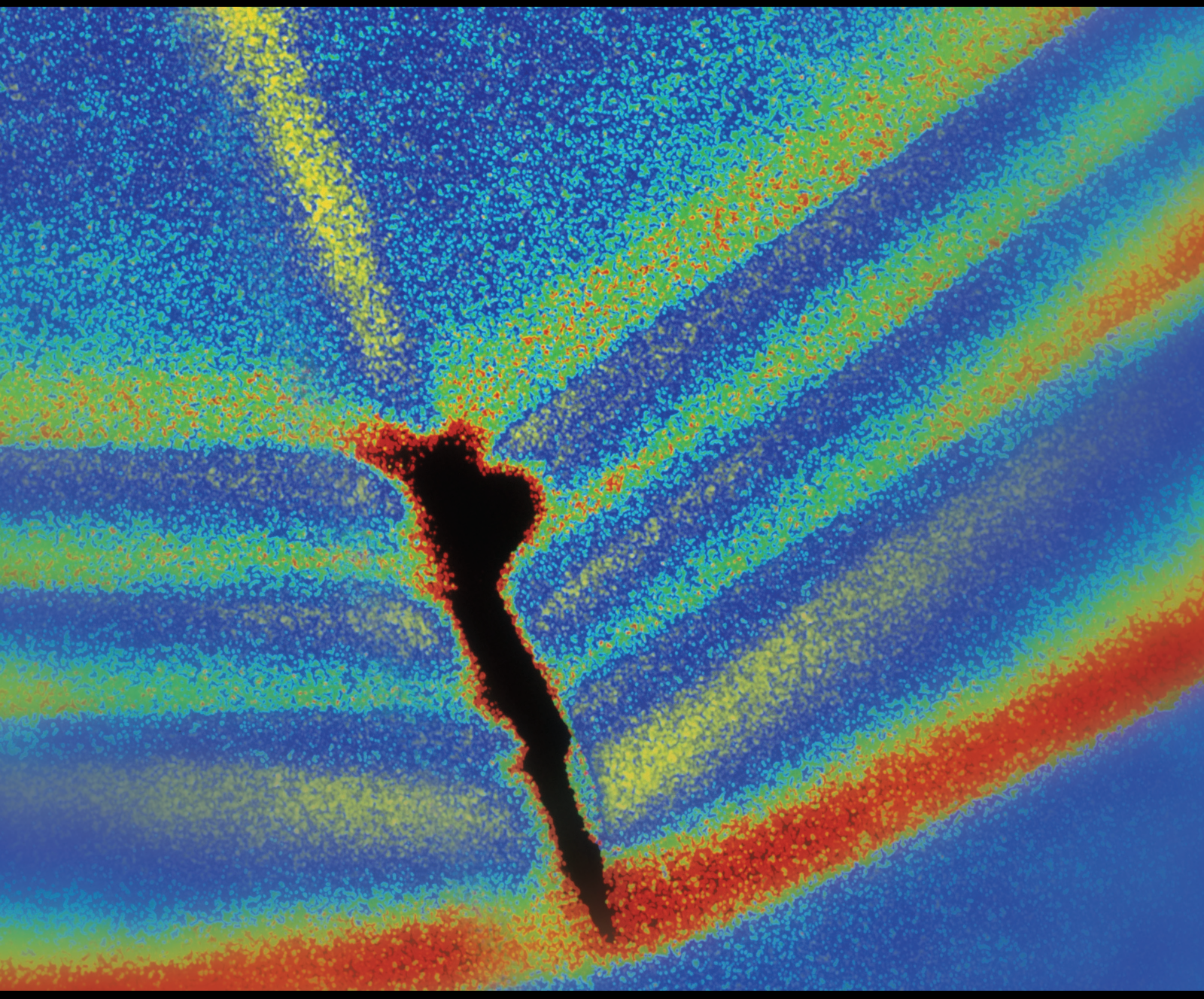

Vibration Analysis and Control of Time-Varying Systems

Shock and Vibration

Vibration Analysis and Control of Time-Varying Systems

Lead Guest Editor: Xiao-ting Rui
Guest Editors: Dieter Bestle, Chuanzeng Zhang, Xuping Zhang, Pierangelo Masarati, and Chengzhi Yuan

Contents

Hindawi
Shock and Vibration
Volume 2021, Article ID 5627734, 15 pages
https://doi.org/10.1155/2021/5627734

Research Article

Research of Mechanical Resonance Analysis and Suppression Control Method of the Servo Drive System

Wenli Li,[1] Yongkang Liu,[1] Shuaishuai Ge,[1] and Daming Liao[2]

[1]*Key Laboratory of Advanced Manufacturing Technology for Automobile Parts, Ministry of Education, Chong-qing University of Technology, Chongqing 400054, China*
[2]*Chongqing University of Technology & Tsinghua Automative Research Institute and Linktron Measurement and Control Techology Co., Ltd, Chongqing 400054, China*

Correspondence should be addressed to Shuaishuai Ge; gess@cqut.edu.cn

Received 10 June 2021; Revised 22 November 2021; Accepted 1 December 2021; Published 22 December 2021

Academic Editor: Chuanzeng Zhang

Transmission mechanisms of the servo drive system are not a pure rigid body, and the existence of the elastic transmission mechanisms will make the system generate mechanical resonance. Aiming at mechanical resonance of the servo drive system, the resonance generation mechanism is analyzed, the four-mass model considering the time-varying meshing stiffness of the gear is established, and the influence of different stiffness parameters on the mechanical resonance of the system is researched in this paper. The composite controller of Model Predictive Control (MPC) with Notch Filter is used to simulate the mechanical resonance suppression of the four-mass servo system considering time-varying meshing stiffness, and it is compared with the mechanical resonance suppression method based on Model Predictive Control. The simulation results show that when the step speed is 200 r/min, the overshoot is reduced from 11.6 r/min to 1.1 r/min, which is reduced by 90.5%. Under the impact load condition, from 10 Nm to 30 Nm, overshoot is reduced from 34.3 r/min to 12.8 r/min, reduced by 62%, and torque oscillation is reduced by 81.5%. Therefore, the composite controller of Model Predictive Control with Notch Filter can suppress the mechanical resonance problem effectively, caused by elastic transmission, and improve the robustness of servo drive system.

1. Introduction

Servo drive system is a common electromechanical system, which has the relationship of multiphysical processes and multicomplex parameter coupling. It is widely used in industrial fields such as industrial robots and hydraulic machine tools [1, 2]. During the operation of the servo motor, the torque ripple is transmitted to load through the transmission shaft, gear, and other transmission mechanisms, which will lead to vibration of the drive motor and transmission mechanisms. Owing to the existence of backlash and other factors, vibration will also be produced and transmitted to the drive motor, resulting in the occurrence of coupling vibration and affecting the life of the motor in the process of transmission. Therefore, it is particularly important to deeply analyze and suppress the vibration mechanism of servo drive system.

In early period, the mechanical vibration suppression control method is relatively straightforward, which is to avoid the sudden change of speed. The elastic effect of damping by adding a term is proportional to the differential speed (difference between connecting rod speed and motor speed) simply [3, 4]. However, for reasons of efficiency and cost, it is rarely applied to the industrial field [5].

At present, mechanical vibration suppression methods mainly focus on passive suppression and active suppression. The passive suppression method does not need to import external energy and change the control system structure. Vibration reduction of servo system is by damping energy dissipation device, vibration isolation, or filtering. The frequently used methods include passive damping vibration reduction, insertion of filter, and improvement of the inertia ratio of motor to load [6–9]. In the passive suppression method, it is difficult to improve the inertia ratio of motor-

load. Low-pass filter will bring a certain phase delay, which is easy to make the dynamic characteristics of the system to deteriorate. The insertion of Notch Filter is easy, and it does not require additional feedback links in the system and can achieve better vibration suppression effect [10]. The active suppression method relies on external given command and system response indicators and changes the controller parameters and structure to weaken the mechanical vibration of servo system [11]. Benefiting from the improvement of basic science and computer science, active suppression methods have been developed rapidly, mainly including state observer, active disturbance rejection control, sliding mode control, fuzzy control, and Model Predictive Control [12–15]. In the active suppression method, fuzzy control is easy to simplify complex information and result in the degradation of the precision of the system. Sliding mode control is greatly affected by the switching amplitude of control variables, which is not suitable for the precise control system.

Model Predictive Control can obtain accurate models through analysis techniques and identification methods, which is an effective solution to nonlinear and constrained problems [16]. Model Predictive Control can realize the control and simultaneous optimization of multidimensional variables. The speed regulator and current regulator of the cascade structure are combined into a noncascaded multi-input and multioutput Model Predictive Controller, which can realize the current at the same time in one calculation cycle. The control system combines the three regulators of the original classic control structure into one controller and realizes simultaneous control of current and speed, which significantly simplifies the system structure and eliminates the current hysteresis link that needs to be considered when designing a speed regulator. The noncascaded structure can further improve its dynamic response while retaining the optimized performance of Model Predictive Control and obtain better control performance.

The actual flexible connection part of the servo drive system is very complex. In order to facilitate the analysis and research, the existing research usually assumes that the transmission mechanisms of the flexible link do not have elastic deformation, and the mass is evenly distributed on a long connection shaft, so as to establish a dual inertia system model [17, 18]. The research of mechanical vibration mechanism of double inertia system is not deep enough, and the vibration of transmission device is not considered in detail. In this paper, starting from the coupling mechanism of mechanical and electrical, taking the four-mass servo drive system considering the time-varying meshing stiffness of gear as the research object, the genesis and characteristics of vibration are expounded. On the basis of this, the use of Model Predictive Control does not require accurate mathematical models and can deal with various problems with constraints. The advantages of Notch Filter that can rapidly attenuate the import signal at a specific frequency point. A composite controller combining Model Predictive Control with Notch Filter is used to suppress the mechanical resonance generated by the servo drive system and reduce the damage caused by the mechanical resonance during the operation of the four-mass servo drive system.

2. Model of the Servo System and Vibration Analysis

As shown in Figure 1, the servo drive system is a complex nonlinear system composed of servo motor, transmission system, and load. Considered on the influence of some nonlinear factors of mechanical system, the servo drive system can be regarded as a four-mass system composed of rigid and flexible components. The concentrated mass method is used to establish the servo drive system model considering the single stage spur gear transmission mechanisms.

2.1. Dynamic Model of the Servo System. There are not great differences in magnitude of inertia between motor, gear drive, and load in servo system. Considered on the torsional stiffness and damping of the drive shaft and the moment of inertia of the motor rotor J_e, gear transmission device J_1, J_2 and load J_L comprehensively, the motor rotor, load, and gear transmission device can be regarded as four parts of moment of inertia. Based on Lagrange dynamics analysis and Hooke's law, do the setup as shown in Figure 2 of the servo drive system dynamics model, as shown inwhere θ_e is the rotation angle of the equivalent motor shaft; θ_1 and θ_2 are, respectively, the rotation angles of the main and driven gears in the gear pair; θ_L is the load rotation angle; T_{s1} and T_{s2} are, respectively, the torque borne by the drive shaft; C_1 and C_2 are, respectively, the torsional damping values of input and output shafts; K_1 and K_2 are, respectively, the torsional stiffness of the input and output shafts; T_e and T_L are the electromagnetic torque and load torque of the motor, respectively; R_1 and R_2 are the radius of the gear base circle; and W_d is the gear dynamic meshing force.

$$\begin{cases} J_e\ddot{\theta}_e = T_e - T_{s1}, \\ J_1\ddot{\theta}_1 = T_{s1} - R_1W_d, \\ J_2\ddot{\theta}_2 = R_2W_d - T_{s2}, \\ J_L\ddot{\theta}_L = T_{s2} - T_L, \\ T_{s1} = C_1\left(\dot{\theta}_e - \dot{\theta}_1\right) + K_1\left(\theta_e - \theta_1\right), \\ T_{s2} = C_2\left(\dot{\theta}_2 - \dot{\theta}_L\right) + K_2\left(\theta_2 - \theta_L\right), \end{cases} \tag{1}$$

2.2. Torsion Dynamics Model of Gear. Only considering the torsional vibration of the gear, ignoring the lateral and axial elastic deformation of the transmission shaft and the elastic deformation of the supporting system, the torsional vibration analysis model of the single stage spur gear transmission is established as shown in Figure 3.

The torsional dynamics analysis model of the gear is shown in

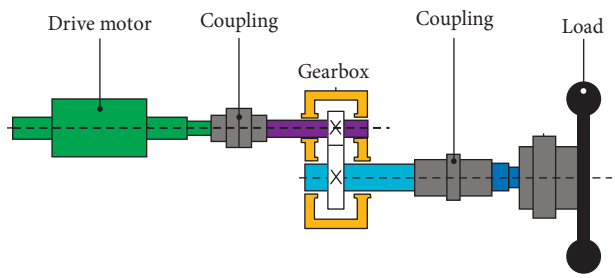

Figure 1: Servo drive system.

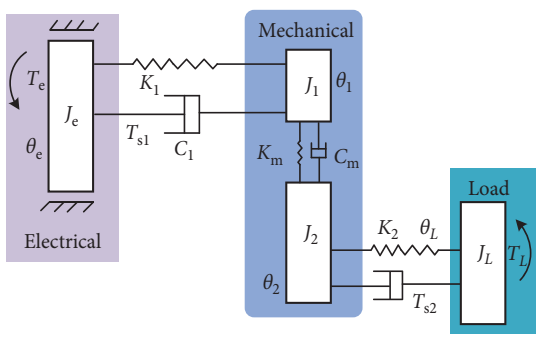

Figure 2: Electromechanical coupling dynamics model.

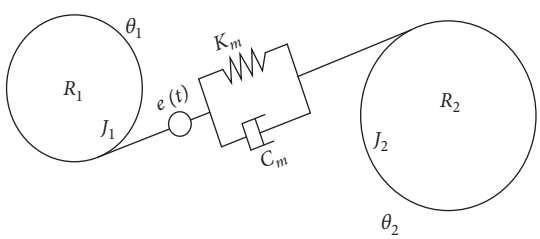

Figure 3: Torsional vibration model of gear transmission.

$$\begin{aligned} &J_1\ddot{\theta}_1 + R_1C_m\left[R_1\dot{\theta}_1 - R_2\dot{\theta}_2 - \dot{e}(t)\right] \\ &\quad + K_mR_1f\left[R_1\theta_1 - R_2\theta_2 - e(t)\right] = T_1, \\ &J_2\ddot{\theta}_2 - R_2C_m\left[R_1\dot{\theta}_1 - R_2\dot{\theta}_2 - \dot{e}(t)\right] \\ &\quad - K_mR_2f\left[R_1\theta_1 - R_2\theta_2 - e(t)\right] = -T_2, \end{aligned} \tag{2}$$

where C_m is the meshing damping of the gear pair; K_m is the time-varying meshing stiffness in the gear transmission process; $e(t)$ is the comprehensive error of the gear meshing; and T_1 and T_2 are the main and driven gears to bear the torque.

According to the aforementioned gear dynamic model, the dynamic meshing force acting on the i-th tooth is shown in

$$W_d = C_m\left[R_1\dot{\theta}_1 - R_2\dot{\theta}_2 - \dot{e}(t)\right] + K_mf\left[R_1\theta_1 - R_2\theta_2 - e(t)\right]. \tag{3}$$

2.2.1. Calculation of Time-Varying Meshing Stiffness. In the process of gear meshing, single and double tooth pairs of gears alternate with the meshing periodically, which results in periodic changes in the comprehensive meshing stiffness of the gears, which causes dynamic excitation of the gear system. The load required to produce a deflection of 1 μm on an average of 1 mm tooth width is called the meshing stiffness of the gear teeth [19]. Therefore, the establishment of a more practical stiffness model and the study of meshing stiffness are of great significance. At present, the meshing stiffness model is mainly obtained by the following two methods:

(1) *Formula Methods.* This method mainly includes Ishikawa formula and its improved algorithm, potential energy method and improved energy method, and Weber formula.

(2) *Finite Element Method.* The finite element method is the most widely used method currently. An empirical formula that can approximate the stiffness can be obtained through the calculated finite element analysis results.

The potential energy method [20] uses the idea of variable increment infinite approximation to calculate the position of each meshing point in the gear meshing process, mapping each meshing point position to a single tooth profile, and using the material mechanics cantilever beam theory to calculate the time-varying meshing stiffness of the gear, which has high calculation efficiency. The result is accurate and includes other advantages. In this paper, the potential energy method is used to solve the time-varying meshing stiffness of gears. During the gear meshing process, the force on the gear teeth can be equivalent to the force on the cantilever beam. The equivalent force model of the spur gear is shown in Figure 4. In the figure, F is the normal load received by the spur gear, and α is the pressure angle. h is half the tooth thickness, where the load F is applied; d is the distance from the root circle to the addendum circle.

According to the knowledge of mechanics, the deformation of the gear teeth under the action of the normal load F on the spur gear can be equivalently decomposed into bending deformation, shear deformation, and radial deformation along the tooth height direction. Based on the theory of material mechanics, the bending stiffness K_b, the shear stiffness K_s, the radial compression stiffness K_r, the stiffness K_d produced by the deformation of the gear teeth, and the stiffness K_h produced by the Hertz contact deformation can be obtained. Therefore, the meshing stiffness of single tooth pair of spur gear pair is expressed as

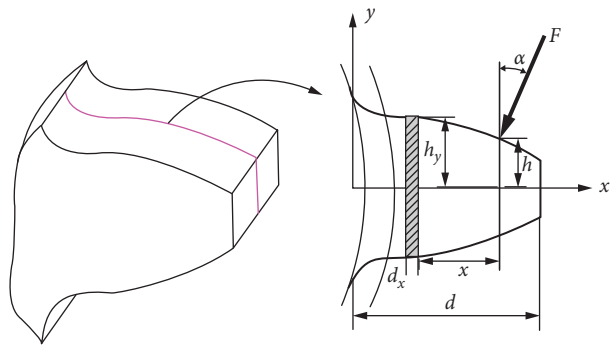

Figure 4: Equivalent model of the spur gear.

$$\frac{1}{K_m} = \frac{1}{\sum_{i=1}^{2}\left(1/K_{bi} + 1/K_{si} + 1/K_{ri} + 1/K_{di} + 1/K_{hi}\right)}, \quad (4)$$

where

$$\frac{1}{k_b} = \begin{cases} \displaystyle\int_{\alpha_1}^{-\alpha_2} \frac{3\{1+\cos\alpha_1[(\alpha_2-\alpha)\sin\alpha - \cos\alpha]\}^2(\alpha_2-\alpha)\cos\alpha}{2\mathrm{EL}[\sin\alpha + (\alpha_2-\alpha)\cos\alpha]^3}\mathrm{d}\alpha + \int_0^{R_b-R_d} \frac{[(\mathrm{d}+x)_1(\cos\alpha_1 - h\sin\alpha)]}{\mathrm{EI}_{x_1}}\mathrm{d}x_1 & Z<42 \\ \displaystyle\int_{\alpha_1}^{-\alpha_3} \frac{3\{1+\cos\alpha_1[(\alpha_2-\alpha)\sin\alpha - \cos\alpha]\}^2(\alpha_2-\alpha)\cos\alpha}{2\mathrm{EL}[\sin\alpha + (\alpha_2-\alpha)\cos\alpha]^3}\mathrm{d}\alpha & Z\geq 42 \end{cases},$$

$$\frac{1}{k_s} = \begin{cases} \displaystyle\int_{-\alpha_1}^{\alpha_2} \frac{1.2(1+\mu)(\alpha_2-\alpha)\cos\alpha\cos^2\alpha_1}{EL[\sin\alpha + (\alpha_2-\alpha)\cos\alpha]}\mathrm{d}\alpha + \int_0^{R_b-R_d} \frac{(1.2\cos\alpha_1)^2}{GA_{x_1}}\mathrm{d}x_1 & Z<42 \\ \displaystyle\int_{-\alpha_1}^{\alpha_3} \frac{1.2(1+\mu)(\alpha_2-\alpha)\cos\alpha\cos^2\alpha_1}{EL[\sin\alpha + (\alpha_2-\alpha)\cos\alpha]}\mathrm{d}\alpha & Z\geq 42 \end{cases}, \quad (5)$$

$$\frac{1}{k_d} = \frac{\cos^2\alpha}{EL}\left\{L\left(\frac{\mu_f}{S_f}\right)^2 + M\left(\frac{\mu_f}{S_f}\right) + P\left(1+\mathrm{Q}\tan^2\alpha\right)\right\},$$

$$\frac{1}{k_r} = \begin{cases} \displaystyle\int_{-\alpha_1}^{\alpha_2} \frac{(\alpha_2-\alpha)\cos\alpha\sin^2\alpha_1}{2EL[\sin\alpha + (\alpha_2-\alpha)\cos\alpha]}\mathrm{d}\alpha + \int_0^{R_b-R_d} \frac{(\sin\alpha_1)^2}{EA_{x_1}}\mathrm{d}x_1 & Z<42 \\ \displaystyle\int_{-\alpha_1}^{\alpha_3} \frac{(\alpha_2-\alpha)\cos\alpha\sin^2\alpha_1}{2EL[\sin\alpha + (\alpha_2-\alpha)\cos\alpha]}\mathrm{d}\alpha & Z\geq 42 \end{cases},$$

where $i = 1, 2$ are the main and driven gears, respectively, α is the pressure angle, G is the shear modulus of elasticity, and $A_x = 2h_xL$ is the gear cross-sectional area.

Based on the distribution of the aforementioned gear pairs in a meshing period, MATLAB programming can be used to obtain the single-double-tooth meshing comprehensive stiffness of the spur gear pair in a period as shown in Figure 5.

2.3. Mechanical Resonance Analysis. Servo drive system has many vibration characteristics during operation. This paper mainly discusses the characteristic vibration of torsional vibration generated by the electromechanical system.

The mechanical rotor is an elastic body, so in the process of rotation, various rotating parts will form different degrees of torsional vibration. Torsional vibration may originate

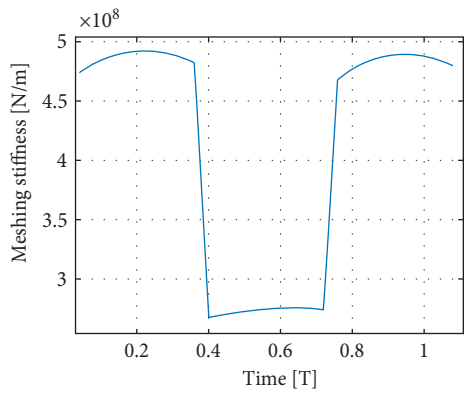

Figure 5: Time-varying mesh stiffness of gears.

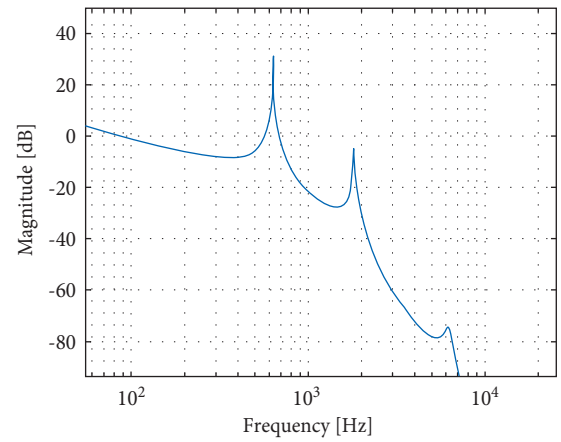

Figure 6: Bode diagram of the system with fixed stiffness.

from the instability of the motor output or load, or it may originate from the internal excitation of the transmission system. These external and internal disturbances lead to forced vibration or free vibration of the mechanical system.

During the operation of the servo drive system, the drive motor directly drives the input shaft to rotate, and the shaft and gear pair are transmitted to the load. During the rotation process, each component will produce a certain degree of elastic deformation, forming an angular deviation, which makes the mechanical transmission system torsionally vibrate. This torsional vibration is mainly reflected in the fluctuation of angle, angular velocity, and angular acceleration.

2.3.1. Mechanical Resonance Analysis with Fixed Stiffness. With analysis of time-varying meshing stiffness, the average meshing stiffness of the gear is 3.8×10^8 N/m. Therefore, the meshing stiffness of the gear pair is equivalent to a fixed stiffness of 3.8×10^8 N/m. The Bode diagram shown in Figure 6 of the four-mass servo system can be obtained using Equation (1).

The four-mass servo system has three resonant frequency points, which are the input shaft, output shaft, and gear pair in the system, and all introduce the corresponding mechanical resonance to the system. The transfer function between the system motor speed and electromagnetic torque can be expressed as

$$\frac{\omega_e(s)}{T_e(s)} = \frac{1}{J_e s} \prod_{n=1}^{3} \frac{s^2 + 2\xi_{an}\omega_{an} + \omega_{an}^2}{s^2 + 2\xi_{bn}\omega_{bn} + \omega_{bn}^2}, \tag{6}$$

where ω_{bn} and ω_{an} are the resonant frequency and antiresonant frequency of the nth resonant link, respectively; and ξ_{bn} and ξ_{an} are the resonant damping coefficient and antiresonant damping coefficient of the nth resonant link, respectively.

The transfer function of four-mass system that brings mechanical resonance is given by Equation (6):

$$G(s) = \prod_{n=1}^{3} \frac{s^2 + 2\xi_{an}\omega_{an} + \omega_{an}^2}{s^2 + 2\xi_{bn}\omega_{bn} + \omega_{bn}^2}. \tag{7}$$

The analysis of Equation (6) shows that the resonance frequency of the system is related to the stiffness coefficient of the transmission mechanism and the equivalent inertia of each part of the system.

In order to investigate the speed control performance of the load, assume that the meshing fixed stiffnesses are 3×10^7, 3×10^8, and 3×10^9 N/m, and the rest of the system parameters remain unchanged. The Bode diagram of the input to the output with the four-mass servo system can be obtained as shown in Figure 7. It can be seen that the change of the fixed stiffness value will change the resonant frequency of the system; that is, the resonant frequency value of the system will increase with the increase of the fixed stiffness.

2.3.2. Analysis of Mechanical Resonance with Time-Varying Meshing Stiffness. In order to further investigate the influence of the time-varying meshing stiffness on the mechanical resonance of the four-mass servo system, the change range of the resonance frequency within the range of the time-varying meshing stiffness is analyzed. Here, the different stiffness values (2.7×10^8,3.8×10^8 and 4.9×10^8 N/m) during the gear meshing process are taken. The Bode diagram of the input electromagnetic torque to the output load speed can be obtained as shown in Figure 8. It can be seen that the mechanical resonance frequency range brought about by the time-varying meshing stiffness is from 5966 Hz to 7638 Hz.

According to Equation (1), a four-mass servo system model considering the time-varying meshing stiffness of gear is established. The servo system model established is compared and analyzed under the conditions of time-varying meshing stiffness and constant stiffness. When a speed command of 1000 r/min is given, the time domain characteristics of the torque transmitted at the load are obtained in Figure 9, and when considering the time-varying stiffness parameters, the system load transfer torque will produce greater fluctuations than considering the constant stiffness parameters. From the resonance analysis of the system under constant stiffness and variable stiffness parameters, it can be concluded that it is necessary to consider the gear meshing

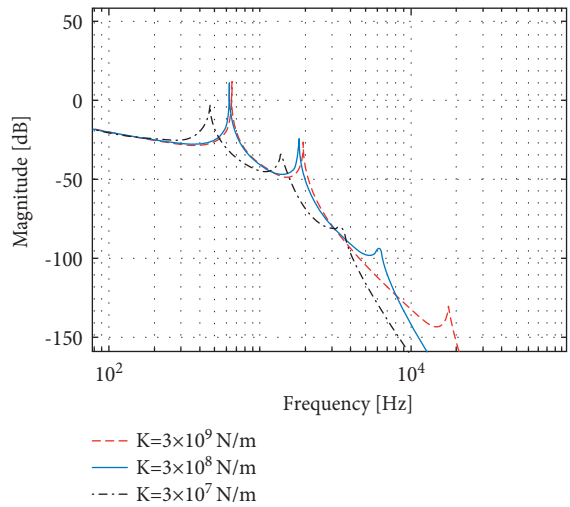

Figure 7: Bode diagram of the servo system with different stiffnesses.

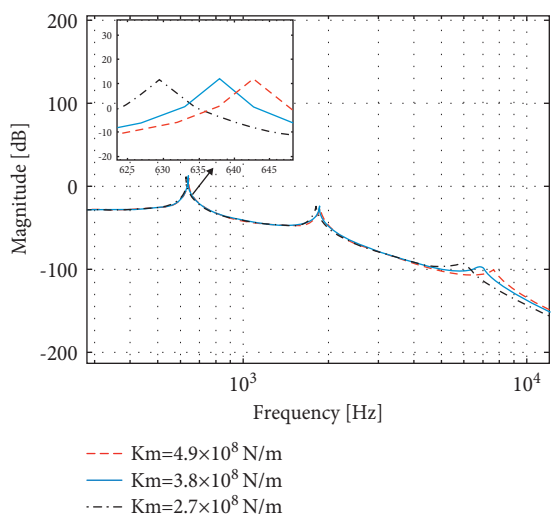

Figure 8: Bode diagram of electromagnetic torque to load speed.

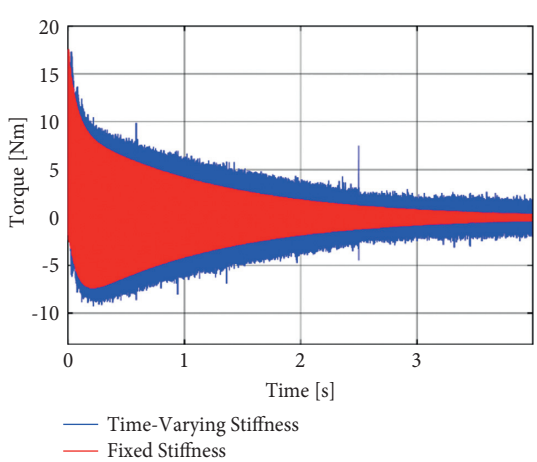

Figure 9: Transmit torque T_{s2} change of the servo system under constant stiffness and variable stiffness.

stiffness as a time-varying meshing stiffness when we research four-mass servo system.

3. Design of the Composite Controller

In the servo drive system, the drive motor, gear transmission, and the load are connected by a transmission shaft. The transmission shaft has certain elasticity. When the transmission shaft is torsionally deformed, a certain torque will be generated. This torque can be regarded as load torque or driving torque [21]. The electromagnetic torque T_e provided by the motor and the torque when the transmission shaft is twisted and deformed together act on the motor shaft. Most transmission devices can be regarded as elastic elements, and all have their own resonant frequency. The existence of elastic elements will bring in one or even several resonance points in the system, which will aggravate the occurrence of mechanical resonance. The structure diagram of the composite controller system is shown in Figure 10.

3.1. Model Predictive Control. Most of the control methods of servo drive systems are based on cascade structure. This structure has multiple PI regulators with cascaded control loops, which are used for three-loop control of current loop, speed loop, and position loop. The cascaded vector control structure is relatively simple and widely used in the industry, but it also has its shortcomings.

The first problem is that the vector control structure of the classic cascaded permanent magnet synchronous motor is complicated, and multiple control loops greatly limit the dynamic response of the system, and the dynamic response of the small inertia system cannot be improved; the other problem is the control of a separate control loop, the controller, runs independently, which means that the overall control performance optimization and effective constraint processing are almost impossible. When the microcontroller adjusts the complex control target, the controller cannot meet all the conditions.

Model Predictive Control is, as shown in Figure 11, a form of control, in which the control action is obtained by solving online, at each sampling instant, a finite horizon optimal control problem, in which the initial state is the current state of the plant. Optimization yields a finite control sequence, and the first control action in this sequence is applied to the plant. MPC differs from conventional control, in which the control law is precomputed of line [16]. Compared with PID and Fuzzy control algorithms, Model Predictive Control can handle complex coupling problems such as multi-inputs, outputs, and multivariable coupling [22].

3.1.1. Establishment of the Prediction Model. Considering that the gear meshing stiffness is a time-varying meshing stiffness, the continuous system state space equation of the four-mass servo system can be obtained using Equation (1):

$$\begin{cases} \dot{\mathbf{x}}(t) = \mathbf{A}\mathbf{x}(t) + \mathbf{B}\mathbf{u}(t) + \mathbf{C}\mathbf{d}(t) \\ \mathbf{y}(t) = \mathbf{E}\mathbf{x}(t) \end{cases}, \tag{8}$$

where Select $\mathbf{x} = \begin{bmatrix} \dot{\theta}_e & \dot{\theta}_1 & \dot{\theta}_2 & \dot{\theta}_L & \theta_e & \theta_1 & \theta_2 & \theta_L \end{bmatrix}^T$ is the state variable of system; $\mathbf{u} = T_e$ are the control inputs; and $\mathbf{d} = T_L$ is a measurable amount of external interference, and then the coefficient matrix is as follows:

$$\begin{aligned} A &= \begin{bmatrix} -J_e^{-1}C_1 & J_e^{-1}C_1 & 0 & 0 & -J_e^{-1}K_1 & J_e^{-1}K_1 & 0 & 0 \\ J_1^{-1}C_1 & A_{22} & A_{23} & 0 & J_1^{-1}K_1 & A_{26} & A_{27} & 0 \\ 0 & A_{32} & A_{33} & J_2^{-1}C_2 & 0 & A_{36} & A_{37} & J_2^{-1}K_2 \\ 0 & 0 & J_L^{-1}C_2 & -J_L^{-1}C_2 & 0 & 0 & J_L^{-1}K_2 & -J_L^{-1}K_2 \\ 1 & 0 & 0 & 0 & 0 & 0 & 0 & 0 \\ 0 & 1 & 0 & 0 & 0 & 0 & 0 & 0 \\ 0 & 0 & 1 & 0 & 0 & 0 & 0 & 0 \\ 0 & 0 & 0 & 1 & 0 & 0 & 0 & 0 \end{bmatrix}, \\ \mathbf{A}_{22} &= -J_1^{-1}\left(C_1 + C_m \cdot R_1^2\right); \mathbf{A}_{23} = J_1^{-1} \cdot C_m \cdot R_1 \cdot R_2, \\ \mathbf{A}_{26} &= -J_1^{-1}\left(K_1 + K_m \cdot R_1^2\right); \mathbf{A}_{27} = J_1^{-1} \cdot K_m \cdot R_1 \cdot R_2, \\ \mathbf{A}_{32} &= J_2^{-1} \cdot C_m \cdot R_1 \cdot R_2; \mathbf{A}_{33} = -J_2^{-1}\left(C_2 + C_m \cdot R_2^2\right), \\ \mathbf{A}_{36} &= J_2^{-1} \cdot K_m \cdot R_1 \cdot R_2; \mathbf{A}_{37} = -J_2^{-1}\left(K_2 + K_m \cdot R_2^2\right), \\ \mathbf{B} &= \begin{bmatrix} J_e^{-1} & 0 & 0 & 0 & 0 & 0 & 0 & 0 \end{bmatrix}^T, \\ \mathbf{C} &= \begin{bmatrix} 0 & 0 & 0 & -J_L^{-1} & 0 & 0 & 0 & 0 \end{bmatrix}^T, \\ \mathbf{E} &= \begin{bmatrix} 0 & 0 & 0 & 1 & 0 & 0 & 0 & 0 \end{bmatrix}. \end{aligned} \tag{9}$$

The forward Euler method [23] is used to discretize Equation (8), and the state space equation of the discrete system is obtained as follows:

$$\begin{cases} \mathbf{x}(k+1) = \mathbf{A}_k\mathbf{x}(k) + \mathbf{B}_k\mathbf{u}(k) + \mathbf{C}_k\mathbf{d}(k) \\ \mathbf{y}(k) = \mathbf{E}_k\mathbf{x}(k) \end{cases}, \tag{10}$$

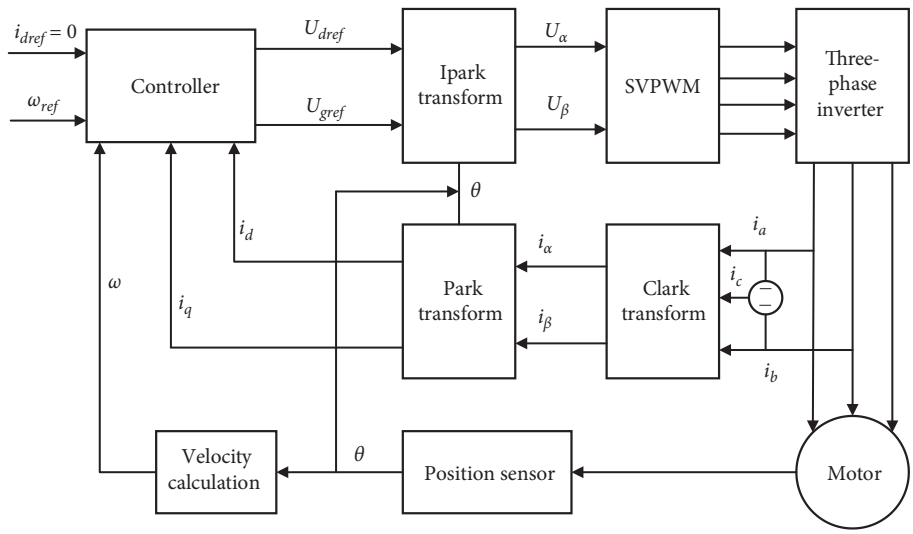

Figure 10: Block diagram of the control system.

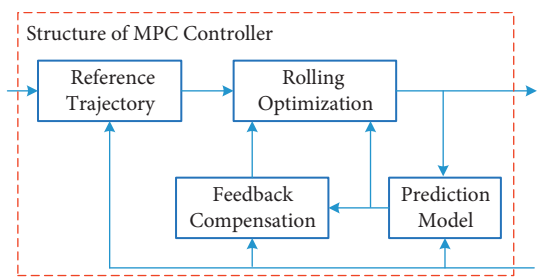

Figure 11: Structure diagram of Model Predictive Control.

where k is the current sampling time and $k+1$ is the next sampling time.

3.1.2. Design of Objective Function. Let $\eta(k) = [\mathbf{x}(k) \;\; \mathbf{u}(k-1) \;\; \mathbf{d}(k-1)]^T$; then Equation (10) can be rewritten as follows:

$$\begin{cases} \boldsymbol{\eta}(k+1) = \widehat{\mathbf{A}}_k \boldsymbol{\eta}(k) + \widehat{\mathbf{B}}_k \Delta\mathbf{u}(k) + \widehat{\mathbf{C}}_k \Delta\mathbf{d}(k) \\ \boldsymbol{\gamma}(k) = \widehat{\mathbf{E}}_k \boldsymbol{\eta}(k) \end{cases}, \tag{11}$$

where $\widehat{\mathbf{A}}_k = \begin{bmatrix} \mathbf{A}_k & \mathbf{B}_k & \mathbf{C}_k \\ \mathbf{0}_{m\cdot n} & \mathbf{I}_m & 0 \\ 0 & 0 & 1 \end{bmatrix}$, $\widehat{\mathbf{B}}_k = \begin{bmatrix} \mathbf{B}_k \\ \mathbf{I}_m \\ 0 \end{bmatrix}$, $\widehat{\mathbf{C}}_k = [\mathbf{C}_k \;\; 0 \;\; 1]^T$, $\widehat{\mathbf{E}}_k = [\mathbf{E}_k \;\; 0 \;\; 0]$, m is the dimension of control quantity, and n is the dimension of state quantity.

Set the predictive horizon as N_p, and control horizon as N_p, $N_c < N_p$. According to Equation (11), the outputs of future prediction of the system can be deduced as follows:

$$\mathbf{Y}(k) = \boldsymbol{\Phi}\boldsymbol{\eta}(k) + \boldsymbol{\Psi}\Delta\mathbf{U} + \Gamma\Delta\mathbf{D}, \tag{12}$$

where $\mathbf{Y}(k) = [\gamma(k+1) \;\; \gamma(k+2) \;\; \cdots \;\; \gamma(k+N_p)]^T$; $\Phi = [\widehat{\mathbf{E}}_k\widehat{\mathbf{A}}_k \;\; \widehat{\mathbf{E}}_k\widehat{\mathbf{A}}_k{}^2 \;\; \cdots \;\; \widehat{\mathbf{E}}_k\widehat{\mathbf{A}}_k{}^{N_p}]^T$; and

$$\boldsymbol{\Psi} = \begin{bmatrix} \widehat{\mathbf{E}}_k\widehat{\mathbf{B}}_k & 0 & 0 & \cdots & 0 \\ \widehat{\mathbf{E}}_k\widehat{\mathbf{A}}_k\widehat{\mathbf{B}}_k & \widehat{\mathbf{E}}_k\widehat{\mathbf{B}}_k & 0 & \cdots & 0 \\ \vdots & \vdots & \vdots & \ddots & \vdots \\ \widehat{\mathbf{E}}_k\widehat{\mathbf{A}}_k^{N_c-1}\widehat{\mathbf{B}}_k & \widehat{\mathbf{E}}_k\widehat{\mathbf{A}}_k^{N_c-2}\widehat{\mathbf{B}}_k & \cdots & \cdots & \widehat{\mathbf{E}}_k\widehat{\mathbf{B}}_k \\ \vdots & \vdots & \vdots & \ddots & \vdots \\ \widehat{\mathbf{E}}_k\widehat{\mathbf{A}}_k^{N_p-1}\widehat{\mathbf{B}}_k & \widehat{\mathbf{E}}_k\widehat{\mathbf{A}}_k^{N_p-2}\widehat{\mathbf{B}}_k & \widehat{\mathbf{E}}_k\widehat{\mathbf{A}}_k^{N_p-3}\widehat{\mathbf{B}}_k & \cdots & \widehat{\mathbf{E}}_k\widehat{\mathbf{A}}_k^{N_p-N_c-1}\widehat{\mathbf{B}}_k \end{bmatrix},$$

$$\Delta\mathbf{U} = [\Delta\mathbf{u}(k) \;\; \Delta\mathbf{u}(k+1) \;\; \cdots \;\; \Delta\mathbf{u}(k+N_c)]^T,$$

$$\Gamma = \begin{bmatrix} \widehat{\mathbf{E}}_k\widehat{\mathbf{C}}_k & 0 & 0 & \cdots & 0 \\ \widehat{\mathbf{E}}_k\widehat{\mathbf{A}}_k\widehat{\mathbf{C}}_k & \widehat{\mathbf{E}}_k\widehat{\mathbf{C}}_k & 0 & \cdots & 0 \\ \vdots & \vdots & \vdots & \ddots & \vdots \\ \widehat{\mathbf{E}}_k\widehat{\mathbf{A}}_k^{N_c-1}\widehat{\mathbf{C}}_k & \widehat{\mathbf{E}}_k\widehat{\mathbf{A}}_k^{N_c-2}\widehat{\mathbf{C}}_k & \cdots & \cdots & \widehat{\mathbf{E}}_k\widehat{\mathbf{C}}_k \\ \vdots & \vdots & \vdots & \ddots & \vdots \\ \widehat{\mathbf{E}}_k\widehat{\mathbf{A}}_k^{N_p-1}\widehat{\mathbf{C}}_k & \widehat{\mathbf{E}}_k\widehat{\mathbf{A}}_k^{N_p-2}\widehat{\mathbf{C}}_k & \widehat{\mathbf{E}}_k\widehat{\mathbf{A}}_k^{N_p-3}\widehat{\mathbf{C}}_k & \cdots & \widehat{\mathbf{E}}_k\widehat{\mathbf{A}}_k^{N_p-N_c-1}\widehat{\mathbf{C}}_k \end{bmatrix},$$

$$\Delta\mathbf{D} = \left[\, \Delta\mathbf{d}(k) \;\; \Delta\mathbf{d}(k+1) \;\; \cdots \;\; \Delta\mathbf{d}\left(k+N_c\right) \,\right]^T, \tag{13}$$

The system control objective is to achieve accurate tracking of load speed without exceeding the maximum allowable electromagnetic torque. The optimization objective function is

$$J(k) = \sum_{i=1}^{N_p} \left\| \mathbf{Y}(k+i|k) - \mathbf{Y}_{\mathbf{ref}}(k+i|k) \right\|_{\mathbf{Q}}^2 + \sum_{i=0}^{N_c-1} \left\| \Delta\mathbf{U}(k+i) \right\|_{\mathbf{R}}^2, \tag{14}$$

where $\mathbf{Y}_{\mathbf{ref}}(k+i|k)$ is the reference value of the system output variable, $(k+i|k)$ represents the system output at time k to predict the value at time $k+1$,where $i = 1, 2, \ldots, N_p$ $\Delta\mathbf{U}(k+i)$ is the time $k+i$ system control input increment, namely, the electromagnetic torque increment, where $i = 0, 1, \ldots, N_c - 1$; Q and R are weight matrices.

3.1.3. Design of Constraint Conditions. Constraints are imposed on the electromagnetic torque, electromagnetic torque increment, and system output of the control input. The constraints of the control input and its increment are

$$\begin{cases} \mathbf{u}_{\min} \le \mathbf{u}(k+i) \le \mathbf{u}_{\max} \\ \Delta\mathbf{u}_{\min} \le \Delta\mathbf{u}(k+i) \le \Delta\mathbf{u}_{\max} \end{cases}, \tag{15}$$

where $\mathbf{u}_{\min}$ and $\mathbf{u}_{\max}$ are the minimum and maximum values of the electromagnetic torque, respectively, and $\Delta\mathbf{u}_{\min}$ and $\Delta\mathbf{u}_{\max}$ are the minimum and maximum values of the electromagnetic torque increment, respectively.

The output constraint condition of system is

$$\boldsymbol{\gamma}_{\min} \le \boldsymbol{\gamma}(k+i) \le \boldsymbol{\gamma}_{\max}, \tag{16}$$

where $\gamma_{\min}$ and $\gamma_{\max}$ are the minimum value and maximum value of system output, respectively.

3.1.4. Optimization Solution. The system optimization problem is that, in the prediction time domain, Equation (14) reaches the minimum under the constraints of Equations (15) and (16). That is, the following problems need to be solved in each control cycle:

$$\min_{\Delta U} J(\boldsymbol{\eta}(k), \Delta\mathbf{U}(k)) \quad \text{s.t.} \begin{cases} \mathbf{U}_{\min} \le \mathbf{S}\Delta\mathbf{U} + \mathbf{U}_t \le \Delta\mathbf{U}_{\max} \\ \Delta\mathbf{U}_{\min} \le \Delta\mathbf{U} \le \Delta\mathbf{U}_{\max} \\ \boldsymbol{\gamma}_{\min} \le \boldsymbol{\gamma}(k+i) \le \boldsymbol{\gamma}_{\max} \end{cases}, \tag{17}$$

where $\mathbf{U}_{\min}$ and $\mathbf{U}_{\max}$ are the minimum value set and the maximum value set of the control quantity, respectively; $\Delta\mathbf{U}_{\min}$ and $\Delta\mathbf{U}_{\max}$ are the minimum value set and the maximum value set of control increment, respectively; and $\mathbf{S} = \mathbf{K} \otimes \mathbf{I}_m$; $\mathbf{U}_t = \mathbf{1}_{N_c} \otimes \mathbf{u}(k-1)$, where $\mathbf{1}_{N_c}$ is the column vector of N_C row, $\mathbf{u}(k-1)$ is the actual control quantity at time k-1, $\otimes$ is the Kronecker product, and

$$\mathbf{K} = \begin{bmatrix} 1 & 0 & \cdots & \cdots & 0 \\ 1 & 1 & 0 & \cdots & 0 \\ 1 & 1 & 1 & \ddots & 0 \\ \vdots & \vdots & \ddots & \ddots & 0 \\ 1 & 1 & \cdots & 1 & 1 \end{bmatrix}_{N_c \times N_c}. \tag{18}$$

By solving the quadratic programming problem, the increment of control input in the control time domain can be obtained as

$$\Delta\mathbf{U} = \left[\, \Delta\mathbf{u}(k) \;\; \Delta\mathbf{u}(k+1) \;\; \cdots \;\; \Delta\mathbf{u}\left(k+N_c-1\right) \,\right]^T. \tag{19}$$

Take out the first item $\Delta\mathbf{u}(k)$ of the control input increment, and the system control input at the current time can be obtained as

$$\mathbf{u}(k) = \mathbf{u}(k-1) + \Delta\mathbf{u}(k). \tag{20}$$

3.2. Notch Filter. There are many uncertainties in the actual operation process, so there will be some errors between the predicted output estimated by the prediction model and the actual output of the system. Due to the nonlinear factor of the time-varying meshing stiffness of the gear pair, the speed deviation (the absolute value of the difference between the actual speed and the given speed) will be large, and the corresponding gain will increase accordingly. At this time, the extracted rotational speed error signal should be processed to reduce the influence of rotational speed fluctuation on the system. Some of Filters can do this well.

Unlike low-pass filters and high-pass filters, the Notch Filter is a circuit that allows only specific frequencies to pass, while effectively suppressing signals at other frequencies. Because of its selectivity to signals, it is widely used in electronic design. It can be divided into two-parameter Notch Filters and three-parameter Notch Filters. Compared with Low-pass Filters and biquad Filters, there are fewer parameters to be determined, and the notch center frequency can be accurately set by Fast Fourier Transform (FFT) to detect the resonant frequency.

The design of the two-parameter Notch Filter is simple, but it only reflects the notch frequency and the width of the notch and cannot control the depth of the notch, so it is easy to attenuate the gain of the system at the notch frequency to no response [24]. In order to improve the performance of the Notch Filter and make up for the deficiencies of the two-parameter Notch Filter, this paper adopts a relatively complete three-parameter Notch Filter.

The transfer function of the three-parameter Notch Filter is shown in

$$G(s) = \frac{s^2 + 2z\omega_n s + \omega_n{}^2}{s^2 + 2p\omega_n s + \omega_n{}^2}. \tag{21}$$

where ω_n is the center frequency of the notch and z and p are the damping ratio coefficients of the notch, respectively.

Figure 12(a) shows the influence of different parameters on the Notch Filter. It can be seen from Figure 12(b) that different systems can choose different notch center frequencies, and unfitting notch depth parameters will also cause frequency signals near the notch center frequency to be filtered out, resulting in system instability. The attenuation amplitude at the notch center frequency ω_n is $|20\lg p/z|$ dB, and the bandwidth is $z\omega_n$. It can be concluded that, compared with the two-parameter Notch Filter, the amplitude attenuation of the three-parameter Notch Filter can be controlled, which can better suppress the mechanical resonance at the resonance point.

3.3. Resonance Suppression Control. By combining the above analysis, mechanical resonance suppression structure block diagram of the four-mass servo drive system is shown in Figure 13. Aiming at the mechanical resonance suppression of time-varying meshing stiffness in this paper, a three-parameter Notch Filter is connected in series to speed feedback loop. Extract the resonant frequency of four-mass servo drive system as the notch center frequency of the Notch Filter by using FFT. The speed will generate the larger gain value at the frequency design, and the difference from the reference value will become a negative gain. The positive gain of transmission mechanisms at the resonant frequency is cancelled, thereby achieving suppression of mechanical resonance. According to Bode diagram of the system, there are three resonance frequency points in the system. The results of FFT analysis of the speed feedback are shown in Figure 14. The resonance frequency near 640 Hz corresponds to the larger positive gain value, which has the greatest impact on the performance of four-mass servo drive system. The results show that it is consistent with Bode diagram analysis. Therefore, it is the basis of the mechanical resonance analysis above, and the mechanical resonance at this resonant frequency point can be suppressed.

4. Simulation Results and Discussion

Compared with the control effect based on MPC, the mechanical resonance suppression control performance of MPC + Notch Filter composite controller for four-mass servo drive system considering time-varying meshing stiffness is proved. The simulation model of four-mass servo drive system and resonance suppression controller are established in Matlab/Simulink. The main parameters of MPC controller are predictive horizon = 25, control horizon = 5, weighting parameter $Q = 0.1$, $R = 1$, and the electromagnetic torque range of the system control input is ±60 Nm. The notch center frequency of the Notch Filter is 637.9 Hz, the notch depth is 20 dB, and notch width is 0.5. The Bode diagram after resonance suppression of system is shown in Figure 15.

The parameters of servo drive system used in the simulation in this paper are shown in Table 1.

4.1. Response Characteristic Analysis of Step Speed. The reference speeds of 0–200r/min and 200–1000r/min were selected for simulation experiments to simulate the speed response of servo drive system at different working conditions. The speed response curves of the two control methods are shown in Figure 16. As shown in the Figure 15(a) and 15(b), with different reference speeds, the MPC + Notch Filter composite controller has small overshoot and great speed following performance. When using MPC method, the oscillation of transfer torque T_{s2} is greater than that of MPC + Notch Filter composite controller. Analysis of the control effect of two control methods is given in Table 2. The speed response time of MPC method is faster than MPC + Notch Filter composite controller, because increasing the filter is equivalent to adding an additional delay link, resulting in a longer response time of the system. The servo drive system requires high accuracy of speed tremble and position offset, but the response time does not affect the control effect of four-mass servo drive system in this paper.

4.2. Dynamic Characteristic Analysis of Impact Load. The operation process of servo drive system is often affected by the impact load. Therefore, it is necessary to analyze the dynamic characteristics of the two control methods with impact load. The reference speed is still set to 1000 r/min.

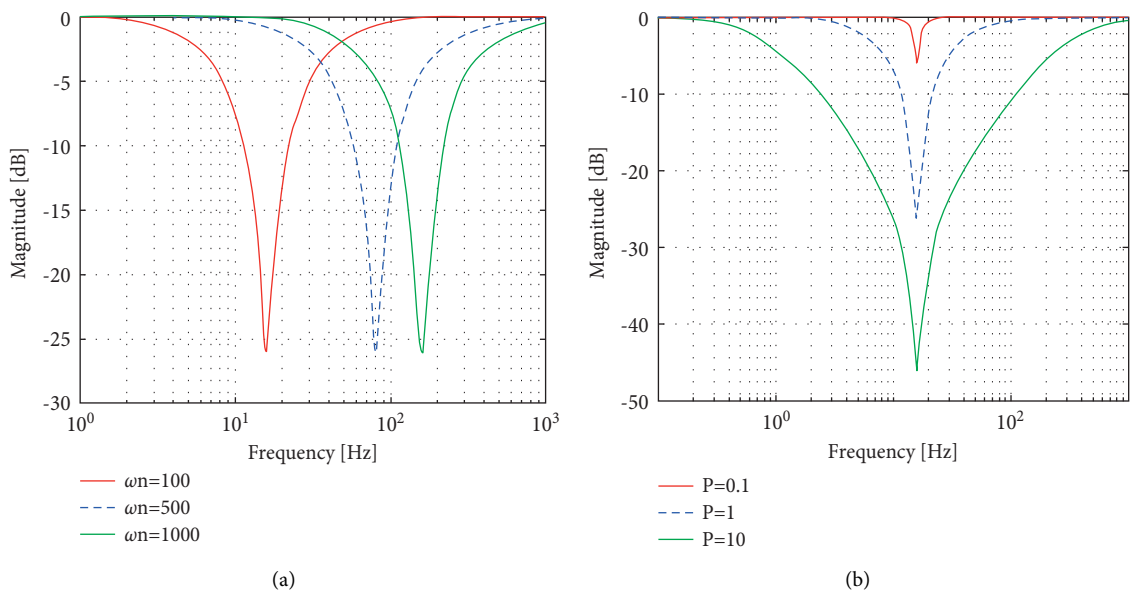

Figure 12: Parametric characteristics of three-parameter Notch Filter. (a) Different notch depths. (b)Different notch center frequencies.

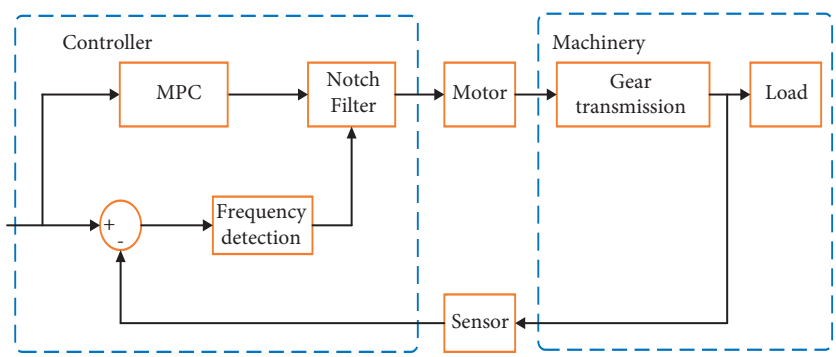

Figure 13: Block diagram of the servo drive system resonant suppression.

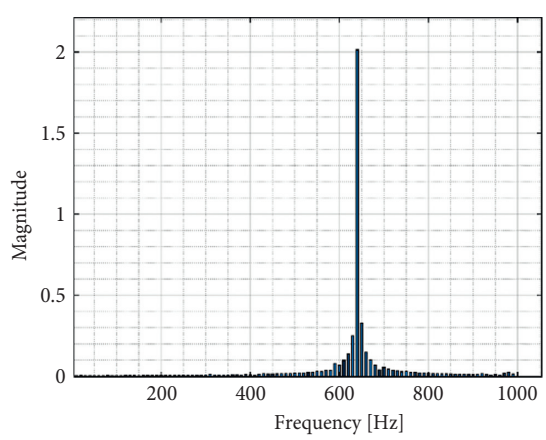

Figure 14: Frequency domain analysis of load feedback speed.

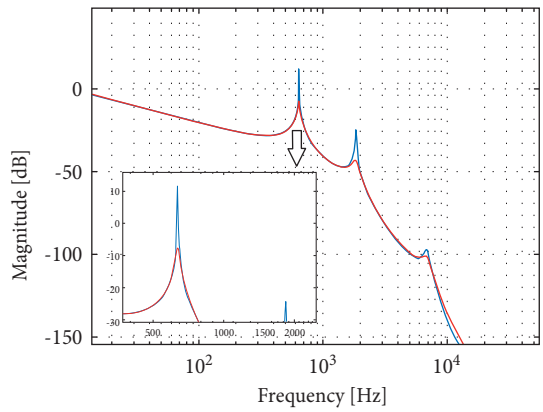

Figure 15: Bode diagram of the system after resonance suppression.

Table 1: Parameters of the servo system.

Parameter names	Values
Rotational inertia of motor/load J_e/J_L(kg·m^2)	$6.15\times10^{-3}/5.75\times10^{-3}$
Rotational inertia of gear J_1/J_2 (kg·m^2)	$2.7\times10^{-4}/2.7\times10^{-3}$
Damping coefficient of shaft C_1/C_2	1
Module of gear m (mm)	3
Pressure angle of gear α (°)	20
Tooth numbers of gear Z_1/Z_2	20/40
Overlap ratio of gear ε	1.6
Reference center distance of gear a (mm)	90
Tooth width W (mm)	20
Yang 's modulus E (PA)	1.9×10^{11}
Poisson ratio v	0.33
Torsional stiffness K_1/K_2 (N·m/rad)	$10^5/10^5$

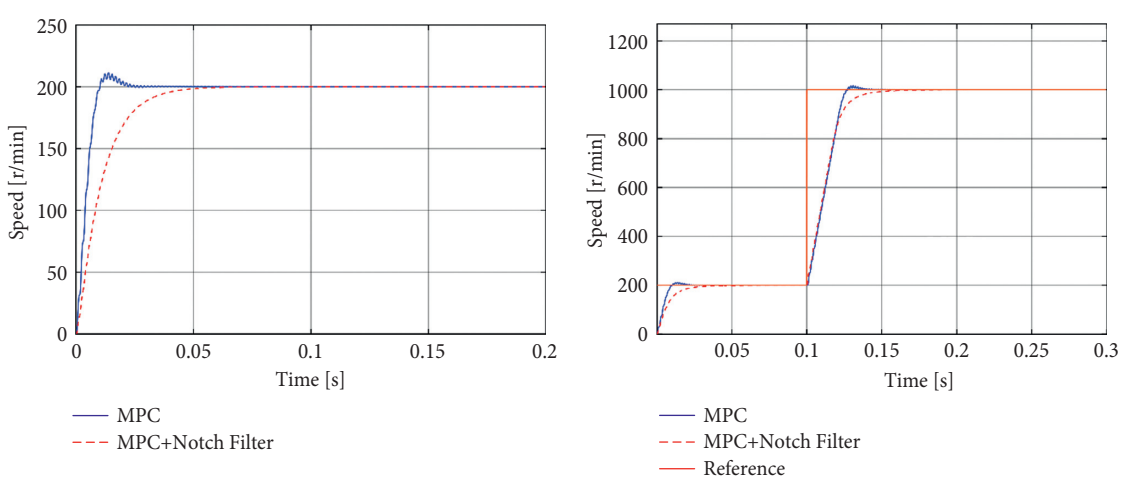

(a) (b)

Figure 16: Continued.

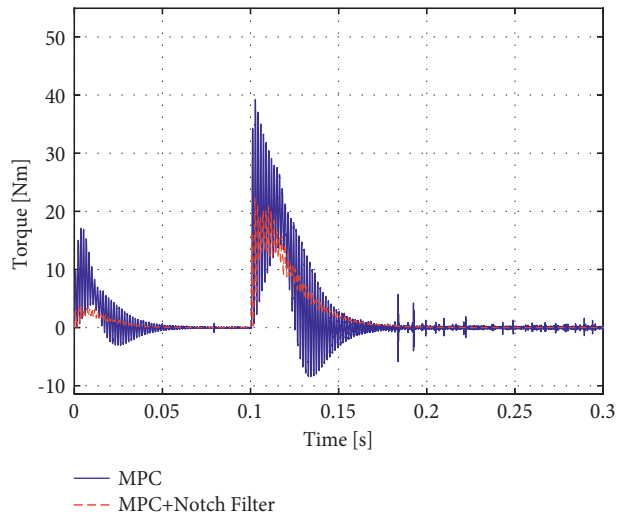

(c)

Figure 16: Dynamic characteristic curve of step speed. (a) Speed response curve of 0–200r/min. (b) Speed response curve of 200–1000r/min. (c) Transfer torque response of load under 200–1000r/min.

Table 2: Comparison of speed response characteristics.

Control method	MPC	MPC + Notch Filter	MPC	MPC + Notch Filter
Speed	0 ~ 200r/min		200 ~ 1000r/min	
Overshoot	11.6r/min	1.1r/min	17r/min	3r/min
Response time	0.04s	0.06s	0.15s	0.18s

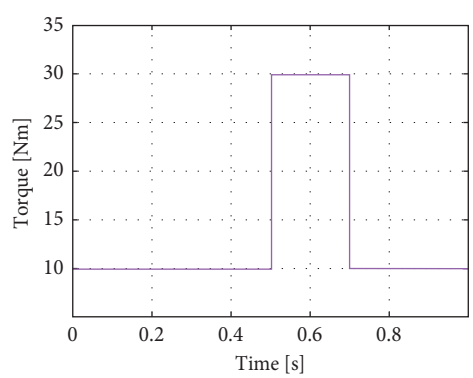

Figure 17: Schematic diagram of the impact load.

The impact load is applied at 0.5 s, and torque increases from 10 Nm to 30 Nm and then recovers to 10 Nm, lasting for 0.2 s. The process is shown in Figure 17.

The simulation results are shown in Figure 18. With the impact load, in order to balance the load, electromagnetic torque suddenly increased and then decreased. The whole process showed two oscillation attenuation phenomena. Table 3 lists some contrast effects with two control methods. The speed response curves of four-mass servo drive system controlled by Model Predictive Control with Notch Filter composite controller also have the advantages of small overshoot and great robustness.

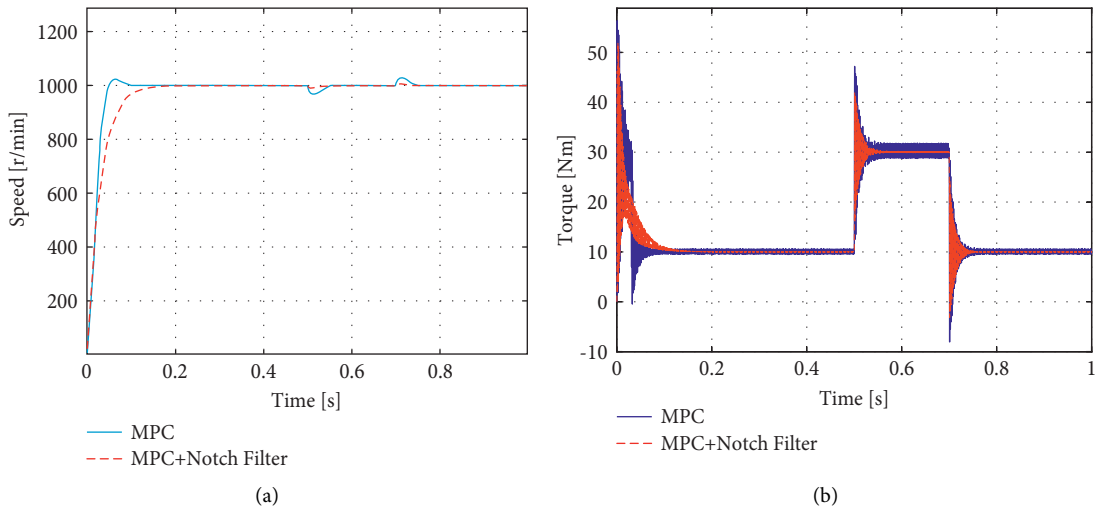

Figure 18: Dynamic response characteristics with impact load. (a) Curve of speed response. (b) Curve of transmission torque T_{s2}.

Table 3: Dynamic characteristics of impact load.

Control method	MPC	MPC + Notch Filter	MPC	MPC + Notch Filter
Torque	10 ~ 30 Nm		30 ~ 10 Nm	
Overshoot	−34.3 r/min	−12.8 r/min	+32 r/min	+10.2 r/min
Torque ripple	0.65 Nm	0.12 N/m	0.68 Nm	0.09 Nm

5. Conclusions

In this paper, a four-mass servo drive system model considering time-varying meshing stiffness of the gear is proposed. The time-varying meshing stiffness will cause a large fluctuation of the transmission torque of the system and bring adverse effects on the dynamic characteristics of system. A mechanical resonance suppression control strategy based on Model Predictive Control with Notch Filter is presented, which is applied to the mechanical resonance suppression of four-mass servo drive system. The control effect of MPC and MPC + Notch Filter under different working conditions (step speed and impact load) is analyzed. The simulation results of this paper show the following:

(1) In the process of step speed response, the composite controller method of Model Predictive Control with Notch Filter can effectively suppress the adverse effects of mechanical resonance on the four-mass servo drive system. When the speed is from 0r/min to 200 r/min, the speed overshoot of the composite controller is 10.5r/min less than that of the MPC controller, and the decrease is 90.5%. When the step speed is from 200r/min to 1000r/min, the speed overshoot of the composite controller is reduced by 14r/min compared with the MPC controller, and the decrease is 82.4%. The speed overshoot is reduced, and the control effect of speed oscillation is better than that of the Model Predictive Control.

(2) In the process from 10 Nm to 30 Nm, the speed overshoot controlled by the composite controller is 12.8 r/min, and the average transmission torque ripple is 0.12 Nm; the speed overshoot controlled by the MPC controller is 34.3 r/min; the average transmission torque ripple is 0.65 Nm. In the process of returning from 30 Nm to 10 Nm, the speed overshoot controlled by the composite controller is 10.2 r/min, and the average transmission torque ripple is 0.09 Nm; the speed overshoot controlled by the MPC controller is 32 r/min; the average transmission torque ripple is 0.68 Nm. The composite controller of Model Predictive Control with Notch Filter can suppress the oscillation of the transmission torque efficiently and have great anti-interference performance and dynamic characteristics.

Data Availability

The characteristics and parameter data of the servo drive system used to support the results of this study are included in this article.

Conflicts of Interest

The authors declare that there are no conflicts of interest regarding the publication of this article.

Acknowledgments

This research was supported by the National Natural Science Foundation of China (Grant nos. 51805061 and 52005067), Natural Science Foundation Project of Chongqing Science and Technology Commission (Grant no. cstc2019jcyj-msxmX0733),

and Youth Project of Science and Technology Research Program of Chongqing Education Commission of China (Grant no. KJQN201901115).

References

[1] K. Pietrusewicz, K. P. Waszczu, and M. Kubicki, "MFC/IMC control algorithm for reduction of load torque disturbance in PMSM servo drive systems," *Applied Sciences*, vol. 9, p. 86, 2019.

[2] G. C. Calafiore and M. C. Campi, "The scenario approach to robust control design," *IEEE Transactions on Automatic Control*, vol. 51, no. 5, pp. 742–753, 2006.

[3] N. C. Singer and W. P. Seering, "Preshaping command inputs to reduce system vibration," *Journal of Dynamic Systems, Measurement, and Control*, vol. 112, p. 1, 1990.

[4] H. Asada, Z. D. Ma, and H. Tokumaru, "Inverse dynamics of flexible robot arms: modeling and computation for trajectory control," *Journal of Dynamic Systems, Measurement, and Control*, vol. 112, pp. 192-193, 1990.

[5] B. R. Murphy and I. Watanabe, "Digital shaping filters for reducing machine vibration," *IEEE Transactions on Robotics and Automation*, vol. 8, no. 2, pp. 285–289, 1992.

[6] Z. Q. Lang, P. F. Guo, and I. Takewaki, "Output frequency response function based design of additional nonlinear viscous dampers for vibration control of multi-degree-of-freedom systems," *Journal of Sound and Vibration*, vol. 332, no. 19, pp. 4461–4481, 2013.

[7] D.-H. Lee, J. H. Lee, and J.-W. Ahn, "Mechanical vibration reduction control of two-mass permanent magnet synchronous motor using adaptive Notch Filter with fast Fourier transform analysis," *IET Electric Power Applications*, vol. 6, no. 7, pp. 455–461, 2012.

[8] J. Tyson and M. Miller, "Evaluating servo system performance," *Control Engineering*, vol. 62, pp. A12–A14, 2015.

[9] A. Annamraju and S. Nandiraju, "A novel fuzzy tuned multistage PID approach for frequency dynamics control in an islanded microgrid," *Int T Electr Energy*, vol. 30, p. 12, 2020.

[10] A. Nehorai, "A minimal parameter adaptive Notch Filter with constrained poles and zeros," *IEEE Transactions on Acoustics, Speech, & Signal Processing*, vol. 33, no. 4, pp. 983–996, 1985.

[11] A. Francesco, M. Angelo, and P. Nicola, "Active vibration control development in ultra-precision machining," *Journal of Vibration and Control*, vol. 27, no. 7-8, pp. 790–801, 2021.

[12] F. Liu, H. Li, L. Liu, R. Zou, and K. Liu, "A control method for IPMSM based on active disturbance rejection control and model predictive control," *Mathematics*, vol. 9, no. 7, p. 760, 2021.

[13] M.-S. Wang and T.-M. Tsai, "Sliding mode and neural network control of sensorless PMSM controlled system for power consumption and performance improvement," *Energies*, vol. 10, no. 11, p. 1780, 2017.

[14] K. Elyaalaoui, M. Labbadi, M. Ouassaid, M. Cherkaoui, and O. Naifar, "Optimal fractional order based on fuzzy control scheme for wind farm voltage control with reactive power compensation," *Mathematical Problems in Engineering*, vol. 3, p. 12, 2021.

[15] I. F. Bouguenna, A. Tahour, R. Kennel, and M. Abdelrahem, "Multiple-vector model predictive control with fuzzy logic for PMSM electric drive systems," *Energies*, vol. 14, no. 6, p. 1727, 2021.

[16] J. B. Rawlings and D. Q. Mayne, *Model Predictive Control: Theory and Design*, pp. 236-237, Nob Hill Pubing, LLC, Wisconsin, WI, USA, 2009.

[17] Y. Zhao, X. Liu, and Q. Zhang, "Predictive speed-control algorithm based on a novel extended-state observer for PMSM drives," *Applied Sciences*, vol. 9, no. 12, p. 2575, 2019.

[18] Y. Yan, J. Yang, Z. Sun, C. Zhang, S. Li, and H. Yu, "Robust speed regulation for pmsm servo system with multiple sources of disturbances via an augmented disturbance observer," *IEEE*, vol. 23, no. 2, pp. 769–780, 2018.

[19] A. Kahraman and R. Singh, "Interactions between time-varying mesh stiffness and clearance non-linearities in a geared system," *Journal of Sound and Vibration*, vol. 146, no. 1, pp. 135–156, 1991.

[20] L. Fan, S. Wang, X. Wang, F. Han, and H. Lyu, "Nonlinear dynamic modeling of a helicopter planetary gear train for carrier plate crack fault diagnosis," *Chinese Journal of Aeronautics*, vol. 29, no. 3, pp. 675–687, 2016.

[21] X. P. Li, D. Y. Shang, and R. Z. Chen, "Control strategy of flexible load servo drive system based on manipulator position and position transformation," *Journal of Mechanical Engineering*, vol. 56, pp. 56–69, 2020.

[22] M. M. Morato, J. E. Normey-Rico, and O. Sename, "Model Predictive Control design for linear parameter varying systems: a survey," *Annual Reviews in Control*, vol. 49, pp. 64–80, 2020.

[23] B. Biswas, S. Chatterjee, S. Mukherjee, and S. Pal, "A discussion on euler method: a review," *Electron J Math Anal Appl*, vol. 1, pp. 294–317, 2013.

[24] T.-H. Oh, J.-S. Han, Y.-S. Kim, D.-Y. Yang, S.-H. Lee, and D.-I. D. Cho, "Deep RL based notch filter design method for complex industrial servo systems," *International Journal of Control, Automation and Systems*, vol. 18, no. 12, pp. 2983–2992, 2020.

Hindawi
Shock and Vibration
Volume 2021, Article ID 7724156, 12 pages
https://doi.org/10.1155/2021/7724156

Research Article

Experimental and Numerical Analysis of Torque Properties of Rotary Elastomer Particle Damper considering the Effect of Gap and No Gap between Rotor and Body of the Damper

Allah Rakhio,[1] Yasushi Ido,[1] Yuhiro Iwamoto,[1] and Atsushi Toyouchi[2]

[1]*Department of Electrical and Mechanical Engineering, Nagoya Institute of Technology, Nagoya 466-8555, Japan*
[2]*KYB Cooporation, 25478 Dota, Kani-shi, Gifu 509-0298, Japan*

Correspondence should be addressed to Allah Rakhio; r.allah.778@stn.nitech.ac.jp

Received 26 July 2021; Revised 22 September 2021; Accepted 29 September 2021; Published 18 October 2021

Academic Editor: Xuping Zhang

Particle dampers are devices used to control the vibration of mechanical systems. In this research, prototypes of rotary elastomer particle dampers are experimentally tested considering gap and no gap between shaft and cylinder. There is a gap between the rotor and cylinder in the gap model; particles can move from one chamber to another. There is no space for the particles to move from one chamber to another in the no-gap model. Elastomer particles are soft, and they have different behavior from hard (metallic) particles. Experiments on rotary elastomer particle dampers considering the gap between rotor and cylinder helped investigate the effects of the change in packing fraction, rotational speed, size of elastomers, and the gap between the rotor and the damper body. A numerical simulation approach based on the discrete element analysis method is used to perform a quantitative and qualitative analysis of the rotary elastomer particle damper. The simulation results are in great agreement with the experiment results. It is observed that packing fraction, rotational speed, size of elastomer particles, and the gap between rotor and cylinder play a vital role in producing higher damper torque.

1. Introduction

Vibrations are frequent oscillations of mechanical systems. Most of the case vibrations are unwanted excitations to the mechanical systems. Vibrations can be extremely dangerous for mechanical systems which can severely affect health as well as human lives. In addition, vibrations decrease the efficiency and accuracy of mechanical devices and machines. Researchers have been trying to develop better techniques and methods to suppress unwanted vibrations. The passive vibration damping technique is one of the most suitable solutions in industrial applications of vibration control. Conventional passive damping technique consists of frictional devices, impact dampers, oil dampers, and tuned mass dampers. In conventional dampers, viscoelastic materials are used. Viscoelastic materials degrade and disintegrate with time and environmental temperature. Similarly, the main problem with oil dampers is the leakages. A particle damper is a vibration control device in which different metals, ceramic, tungsten, rubbers, sand, or other types of particles are used. Particle damper controls the vibration of any mechanical system by dissipating the kinetic energy; kinetic energy can be dissipated in two ways in a particle damper, one by friction and second is collisions between particle-particle and particle-wall of the damper.

There are two types of dampers used in the particle-based vibration control system. One is particle impact damper, and the other is the piston and rotor-based particle damper. Particle impact dampers consist of a closed cavity with particles inside it. In piston and rotor-based particle dampers, a moving rod or rotor is used inside the container of the damper. The piston-based particle damper is a linear damper consists of a rod, and a rotary particle damper consists of a rotating shaft.

In recent decades, researchers and scientists turned their focus towards particle dampers due to several advantages of

particle dampers, such as no loss in efficiency at higher temperature [1, 2] and simple construction [3], which results in ease of maintenance and manufacturing [4].

Previous work has mainly focused on using metallic or other hard particles in the particle damper [5]. Marhadi and Kinra proposed a particle damper for beam [6], the effect of packing fraction was investigated. In their experiments, the particles made of lead, steel, tungsten, and glass were used. They argued that the size and the number of particles are the parameters that must be considered while designing particle impact dampers. Sánchez et al. studied the effect of different sizes and shapes of grains; they observed the welding of grains at high temperatures [7]. Liu et al. proposed a method of vibration control of structures with the help of particle dampers; they considered the nonlinear characteristics of the damper [8]. Their investigation proved that the damping is affected by the thickness of the disk cavity. Researchers also used the tungsten powder as a damping medium in the damper [9]. It was shown that packing fraction and container dimension have an enormous influence on the damping capabilities of a damper. Friend and Kinra reported the nonlinear behavior of particle dampers using lead particles [10]. Also, they showed the high damping capability of lead compared to other metallic materials. Fabian et al. showed particle impact damper's applications in automobile applications [11]. They investigated the oil pan noise reduction in a combustion engine using a granular particle damper. Kachare and Bimleshkumar [12] researched on the effect of packing fraction and size of metallic particles; they used 1 mm, 2 mm, and 3 mm diameter spherical shaped particles made of copper. They concluded that 1 mm diameter-sized particle showed better performance than 2 mm and 3 mm diameter particles, and at 50% packing fraction, the damper shows maximum performance; after 50% packing fraction, a decline in damper performance was noticed.

In recent years, elastomer particles have been introduced and studied [1]. Metal particles and elastomer particles are different in nature and properties, so they behave differently in different situations. More importantly, one of the essential advantages of using elastomer particles is noise reduction [13]. Very few articles have been published on the damping behavior of elastomer particles; most of them are considering linear elastomer particle dampers. Morishita et al. proposed a double rod type linear particle damper. They used elastomer particles instead of metallic ones [14]. They reported that the change of packing fraction, frequency, and stroke of the piston changes the damper force. Kawamoto et al. proposed a double rod type linear damper using elastomer particles made of silicon [1]. Kishan et al. investigated torque dependency on the angle of the rotor in a rotary elastomer particle damper [15].

As for our knowledge, no more articles have been found on the damper torque properties of a rotary elastomer particle damper. It is essential to note that hard metallic particles or powders were used in most previous studies. Although the metallic particles are primarily used in the dampers as a vibration suppression medium, the main issue with metallic particles is the high cost and noise due to collisions. In this research, we are using elastomer particles instead of metallic ones. Elastomer particles do not produce noise because of their soft and elastic properties. Several factors can affect the damping performance of particle dampers, such as packing fraction and size of particles. However, due to the change in these parameters, there was a massive change observed in damping properties of damper because these changes can cause a change in the cooperative moment of damping particles [16]. The gap between the rotor and cylinder can also significantly change the cooperative moment of particles inside the damper. The performance of a particle damper is affected by the packing fraction and size of particles [17]. None of the studies examined the role of the gap between the rotor and the cylinder in a rotary elastomer particle damper. So, it is essential to do an in-depth study on the behavior of elastomer particles considering the effect of the gap between the rotor and damper body, which can affect the damping capabilities of a rotary elastomer particle damper. This research provides new insight into the research on particle dampers. In addition, the findings of this research can help academia and industry to design more efficient rotors for particle damper applications. This paper proposes rotary elastomer particle dampers with gap and no gap between rotor and cylinder.

It is expected that the rotary elastomer particle damper with the gap between rotor and cylinder can provide a strong damper torque than the rotary elastomer particle damper with no gap between rotor and cylinder. Rotary elastomer particle damper with no-gap model produces torque due to resistance of particles due to friction and collision between particle-particle and particle-wall of the damper, but in case of rotary elastomer particle damper with gap model, extra layers of strongly compressed elastomer particles can enter the gap between the rotor and the body. Because of the elastic properties of the elastomer particles, the particles in the gap region can provide high repulsive forces in the motion of the rotor. There is a direct correlation between repulsive forces from the particles and damper torque.

In this study, the damper torque characteristics of rotary elastomer particle damper were investigated. The effects of packing fraction, rotor speed, size of elastomer particles, and the gap between rotor and cylinder on damper torque were examined. The behavior of elastomer particles inside the damper was analyzed by numerical simulations using the discrete element method.

2. Experiments

2.1. Fabrication of Elastomer Particles. TSE3466 (produced by Momentive Performance Materials) is the main ingredient for preparing silicon rubber particle samples. TSE3466 has a hardness of 60, the density is 1.10 kg/m^3, and the tensile strength (MPa) is 7.4. TSE3466-A is the primary raw material, but it is mixed with TSE3466-B, with a ratio of 10 : 1. Product B worked as a catalyst, and its job is to speed up the drying procedure. Before the molding, the air from the raw material was removed by a vacuum chamber. In the next step, we removed the dried elastomers from the molds after 24 hours. We prepared elastomer particles of 3 mm, 4 mm,

and 5 mm diameter for experimental purposes. The main reason to select particles of 3 mm, 4 mm, and 5 mm diameter is the expected higher damper torque of the damper due to higher deformation range comparing to particles of 2 mm and 1 mm diameter. Qualitative analysis of 3 mm, 4 mm, and 5 mm diameter particles is more accessible than smaller particles. Fabrication of 1 mm and 2 mm diameter particles is more complex than the 3 mm diameter particles; it takes a long time to remove smaller size particles from the molds. Figure 1 shows the prepared samples after being removed from the molds. Figure 1 shows the sample of a spherical particle of 3 mm, 4 mm, and 5 mm diameter particles made from TSE3466.

2.2. Damper Construction and Working. The schematic diagram of the damper used in this experiment is shown in Figure 2; the damper consisted of the body, cover, rotor, holder, shaft, and bearings. All dimensions in the figure are in millimeters (mm). Two different types of rotors were used, as shown in Figure 2. In this damper, the holder's job was to hold the damper while performing experiments; it stopped the damper body from rotation. There were two tapered roller bearings (NTN30202) used in the damper, which supported the rotor of the damper. The parts other than the bearings were made of stainless steel SAE304. The damper was tested with no particles inside, and it produced no damping torque, so it can be stated that bearings and damper parts do not affect the test results. In the study, the effect of packing fraction on the rotary elastomer particle damper is analyzed. The packing fraction = total mass of particles/(density of particles and volume of the damper container). The working mechanism of the damper is simple. As the force applied to the rotor of the damper, the rotor started to move. As the rotor moved, it pushed the elastomer particles to move in the direction of the rotor. The main reason behind selecting this damper is its simple working mechanism, which helped to understand and answer the article's primary research question. This damper size is suitable for several mechanical engineering applications, i.e., car seat suspension or automobile door closer. In the future, the prototype can easily be tested for practical application due to its small size.

2.3. Experiential Setup and Experimental Conditions. The damper torque of the designed elastomer particle damper is measured experimentally using an experimental setup shown in Figure 3. This test setup consists of a servo motor (Model-NXM920A-PS10) from Oriental Motors Co., Ltd., Japan. The experimental setup has rotational speed ranging from 0 to 120 rpm of the shaft. Couplings are used to connect the damper shaft with the shaft of the test setup. The torque meter used in the experiment is of UTM II from Unipulse Corporation with a torque monitoring capacity of 10 Nm. The torque meter measured the resistive torque generated by the damper. A control unit is used to control the rotation of the motor. The interface is used to provide the torque readings from the torque meter and transfer them to the computer. The maximum standard deviation was 0.13 (Nm).

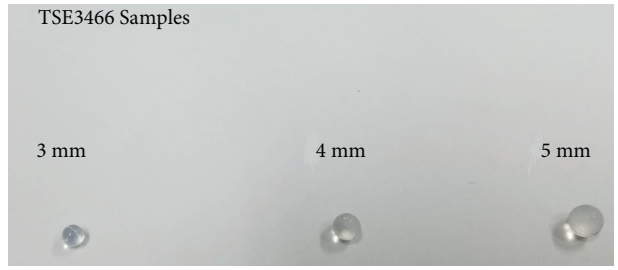

Figure 1: Elastomer samples of TSE3466 3 mm, 4 mm, and 5 mm diameter particles after being removed from molds.

Initially, 5 to 6 revolutions at high rpm were given to the shaft to settle down the particles at random locations. The temperature of the cylinder of the damper was monitored during the experiments; few degrees rise in temperature was detected; however, it did not change the mechanical properties of TSE3466, so the effect of temperature can be neglected.

3. Numerical Simulation of the Rotary Elastomer Particle Damper

The discrete element method (DEM) is used to simulate the particle behavior inside the rotary elastomer particle damper. In DEM, the collision between the particle-particle and particle-wall is modeled based on contact force laws. The DEM simulation provides a much satisfying insight into the particle governing process. The DEM simulations can enhance basic understanding of particle behavior, as well as it can help to improve the design and efficiency of particle dampers. A theoretical approach was used to prepare this model by considering two particles which we named particle i and particle j.

The basic equations of motions can be stated as

$$m_i \frac{d^2 r_i}{dt^2} = F_i, \qquad I_i \frac{d\Omega_i}{dt} = T_i, \tag{1}$$

where t is the time, m_i is the mass of the particle, r_i is the position vector of the particle i, F_i is the sum of the forces acting on the particle i, I_i is the moment of inertia, Ω_i is the angular velocity vector, and T_i represents the total torque applied on the particles. In these equations, a particle is named particle i, by considering which the model will further progress. F_i, I_i, T_i can be expressed as

$$F_i = F + F_{ct} + F_g, \qquad T_i = r_i \times F_{ct}, \qquad I_i \frac{8}{15} \rho \pi a^5, \qquad F_g = m_i g, \tag{2}$$

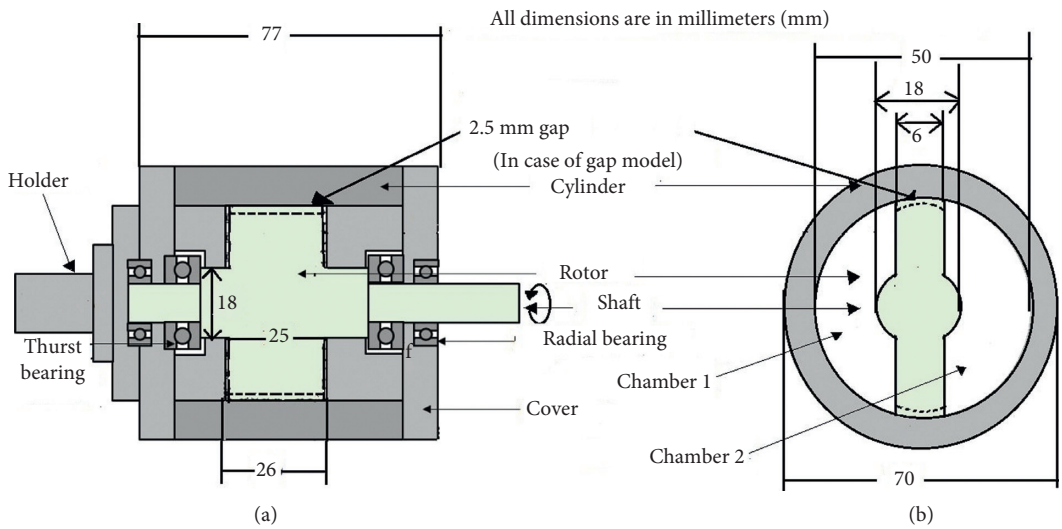

Figure 2: Schematic diagram of the rotary damper with gap and no gap between the rotor and cylinder; all dimensions are in millimeters (mm). (a) Cross-sectional side views of the damper. (b) Cross-sectional top views of the damper.

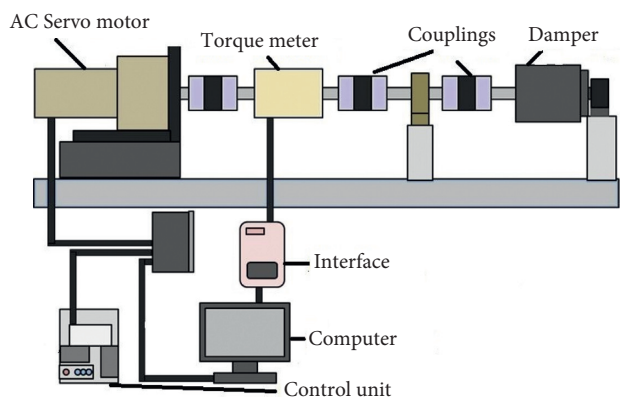

Figure 3: Schematic diagram of experimental setup.

where F_{cn} is the normal contact force between particles or the walls of the damper, F_{ct} is the force in the tangential direction, F_g is the gravity force, g is the gravitational acceleration vector, a is the radius of the elastomer particle, and ρ is the particle density. This model is based on the Kelvin–Voigt material model, which consists of an elastic spring dashpot and slider.

$$F_{cn} = \left(-K_n\delta_n + C_n V_{ij}.n_i\right)n_i,$$
$$F_{ct} = K_t\delta_t + C_t V_{fij}, \tag{3}$$

where the subscript n represents the parameters of normal direction, whereas the subscript t represents the parameters of tangential direction, K_n is the elastic modulus in the normal direction, K_t is the elastic modulus in the tangential direction, C_n is the viscosity coefficient in the normal direction, C_t is the viscosity coefficient in the tangential direction, δ_n is the strain in the normal direction, δ_t is the strain in the tangential direction, n_i is the unit vector in the normal direction from i to particle j, V_{ij} is the relative velocity vector of particle i with respect to particle j, and V_{fij} is the tangential relative velocity.

$$V_{ij} = v_i = v_j,$$
$$V_{fij} = V_{ij} - \left(V_{ij}.n_i\right)n_i + 2a\left(\omega_i - \omega j\right) \times n_i, \tag{4}$$

where ω_i and ω_j are the angular velocity vectors of particles i and j, respectively. Viscosity coefficients in the normal direction C_n and viscosity coefficient in the tangential direction C_t can be represented as [18]

$$C_n = \overline{\alpha}\sqrt{m_i K_n \delta_n^{0.25}},$$
$$C_t = \overline{\alpha}\sqrt{m_i K_n \delta_{ct}^{0.25}}, \tag{5}$$

where δ_{ct} is the displacement in elastomer particle in the tangential direction; $\overline{\alpha}$ determines the magnitude of viscous damper force, which can be expressed by the following equation [18]:

$$\overline{\alpha} = 2.2\sqrt{\frac{\ln\left(e^2\right)}{\ln\left(e^2\right) + \pi^2}}. \tag{6}$$

The elastic modulus in the normal direction is expressed by the following equation based on Hertz's contact theory [18]:

$$\begin{aligned} K_{nij} &= \frac{2}{3\pi}\left(\frac{1}{\delta_i}\right)\sqrt{\frac{a\delta_n}{2}}, \\ K_{niw} &= \frac{4}{3\pi}\left(\frac{1}{\delta_i + \delta_w}\right)\sqrt{a\delta_n}, \\ \delta_i &= \frac{1 - \nu_i^2}{E_i\pi}, \\ \delta_w &= \frac{1 - \nu_w^2}{E_w\pi}, \end{aligned} \tag{7}$$

where the subscript w indicates that the quantities relate to the wall, K_{nij} is the elastic coefficient when particle i and particle j are in contact, whereas K_{niw} is the elastic coefficient when the particle i is in contact with the wall of the damper, E_i and E_w are the moduli of longitudinal elasticity of the particle and wall, respectively, and ν_i and ν_w are the Poisson's ratios of the particle and wall, respectively. Considering that there is no slip at the point of contact, the tangential elastic coefficient can be expressed as the following equation [18]:

$$\begin{aligned} K_{tij} &= \left(\frac{2\sqrt{2a}\,G_i}{2 - \nu_i}\right)\delta_n^{0.5}, \\ K_{tiw} &= \left(\frac{8\sqrt{a}\,G_i}{2 - \nu_i}\right)\delta_n^{0.5}, \end{aligned} \tag{8}$$

where K_{tij} is the elastic coefficient when particle i is in contact with another particle j, K_{tiw} is the elastic coefficient when particle i is in contact with the wall of the damper, and G_i is the transverse elastic modulus of the particle and is expressed as follows [18]:

$$G_i = \frac{E_i}{2\left(1 + \nu_i\right)}. \tag{9}$$

For calculating the time steps of the velocity, displacement, and angular velocity of the particles, the Adams–Bashforth method of second-order accuracy is applied. The analytical model for the rotary elastomer particle damper is the same as the rotary damper prepared for experiments, as shown in Figure 2. The simulations are conducted at the packing fractions of 30%, 40%, 45%, and 50%. The rotational speed of the shaft in the simulation is kept at 60 rpm. The material of the elastomer particles is silicon rubber (TSE3466). The diameter of the elastomer particles used in the numerical simulations is 3 mm. The friction coefficient is 0.5 in this simulation [19], and the time step is 0.0000000075 seconds. The density of the particle is 1.10 kg/m^3. The particle's Poisson ratio and wall's Poisson ratio were 0.5 and 0.3.

One of the limitations of this simulation is long processing time. Data collection of simulation at each packing fraction took around 4 to 5 days. More powerful computers can reduce the computational time of particle-based simulation systems. Advanced and fast parallel processing can make more efficient use of the algorithm.

4. Results and Discussion

4.1. Torque Generation Mechanism of the Rotary Elastomer Particle Damper. We have performed extensive experiments to analyze the damper torque performance of rotary elastomer particle dampers. The qualitative and quantitative analysis of the rotary damper is also performed via numerical simulation. The purpose of the simulation is to allow us to analyze the behavior of the elastomer particles inside the damper. We first present a simulation experiment result to study the behavior of particles, followed by a detailed analysis of the damper torque properties using rotary elastomer particle damper with gap and no-gap model prototypes. Figures 4 and 5 show the torque versus time graph of the gap and no-gap models of the rotary elastomer particle damper. Figures 4 and 5 show the simulation results and the experimental results of rotary elastomer particle damper at 60 rpm and 50% packing fraction using particles of 3 mm diameter. To investigate the effect of particle deformation and particle sliding, decomposition of both the factors based on simulation results is conducted. The decomposition results are taken from 50% packing fraction at 60 rpm, using 3 mm diameter elastomer particles. In Figure 6, the torque due to particle deformation is higher than the torque due to sliding friction. The dominant source of torque generation is particle deformation, so the compression force on particles plays a significant role in producing higher damper torque. Particles under higher compressive forces tend to generate strong repulsive forces in the rotation of the rotor. Due to repulsive forces from the particles, damper torque is produced by the damper.

Figure 7 shows the experimental and simulation results of the torque versus packing fraction curve using elastomer particles of 3 mm diameter in the no-gap model. The results are taken from the rotational speed of 60 rpm. In Figure 7, the simulation results are in good agreement with experimental results. The experimental curve shows slightly higher torque than simulation results; this may be because of the surface roughness factor of the particles, which is not considered in the simulation. In our future research, this difference between experimental and simulation results can be reduced by considering the effect of the surface roughness factor in simulations.

The design with gap and no gap between rotor and cylinder produced no noise during experiments. Due to the elastic nature of elastomer particles, they deform on collision and compression but do not produce noise. Due to the collision between elastomer particles, the sound is inaudible

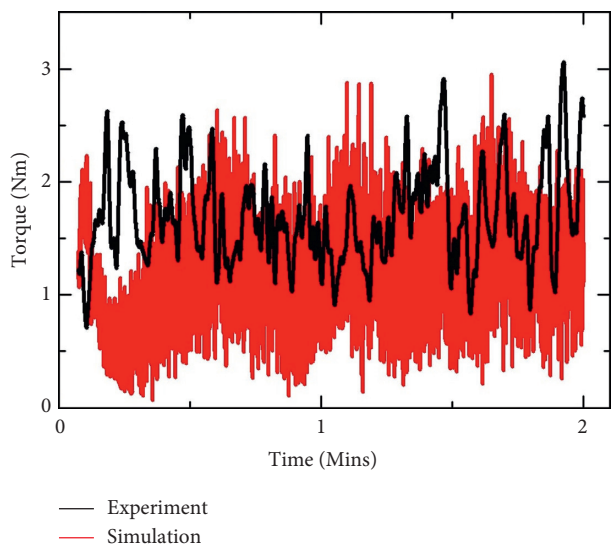

Figure 4: Time history of the rotary damper with a gap model using 3 mm diameter particles; the packing fraction is 50%, and the rotational speed is 60 rpm.

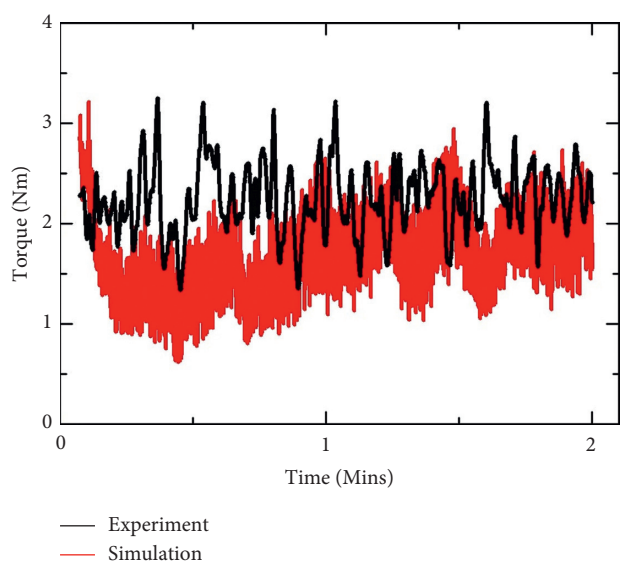

Figure 5: Time history of the rotary damper with a no-gap model using 3 mm diameter particles; the packing fraction is 50%, and the rotational speed is 60 rpm.

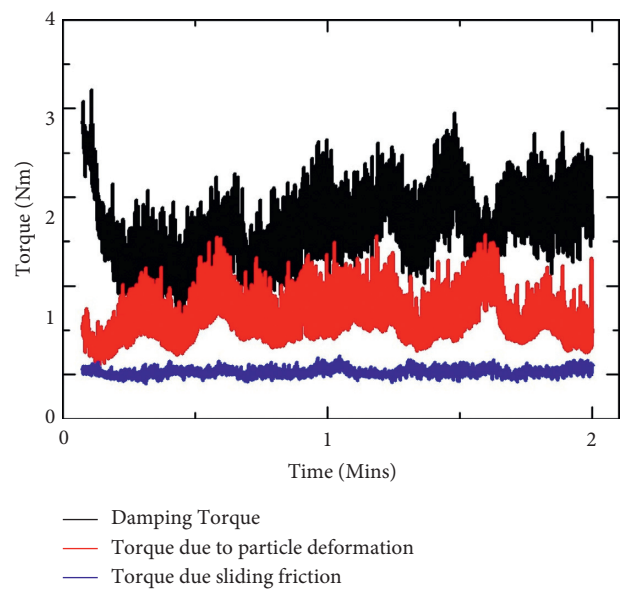

Figure 6: Time history of the rotary damper with a no-gap model using 3 mm diameter particles, decomposition of torque due to particle deformation, and torque due to sliding friction.

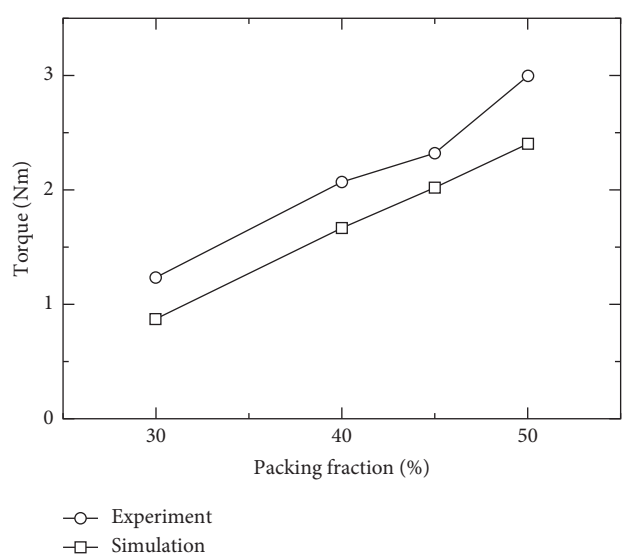

Figure 7: Experimental and simulation results of the torque versus packing fraction curve using elastomer particles of 3 mm diameter in the no-gap model. The rotational speed is 60 rpm.

to humans, but it may be possible to record or measure it using a microphone.

Figures 8 and 9 show the qualitative results obtained from the simulation of rotary elastomer particle damper with no-gap and gap models. To investigate the force of compression on the elastomer particles, the simulation was conducted at 50% packing fraction at the rotational speed of 60 rpm, using 3 mm diameter elastomer particles.

In Figures 8 and 9, the strength of compressive force on the particles depends on the rotor's location inside the cylinder. When the rotor rotates, it forces the elastomer particles to move forward in the direction of the rotor rotation. Particles in front of the rotor push other particles to move forward. The force of compression on the elastomer particles is investigated using simulation results. In Figures 8 and 9, several particles have a strong force of compression near the rotor, due to which a strong repulsive force from the elastomer particles is produced. When the rotor is at the bottom area of the cylinder, the force of compression is strong because the gravitational force is also acting on the particles. The elastic repulsive force of particles is produced by the collision of elastomer particles and frictional forces between particle-particle and particle-wall. It is important to

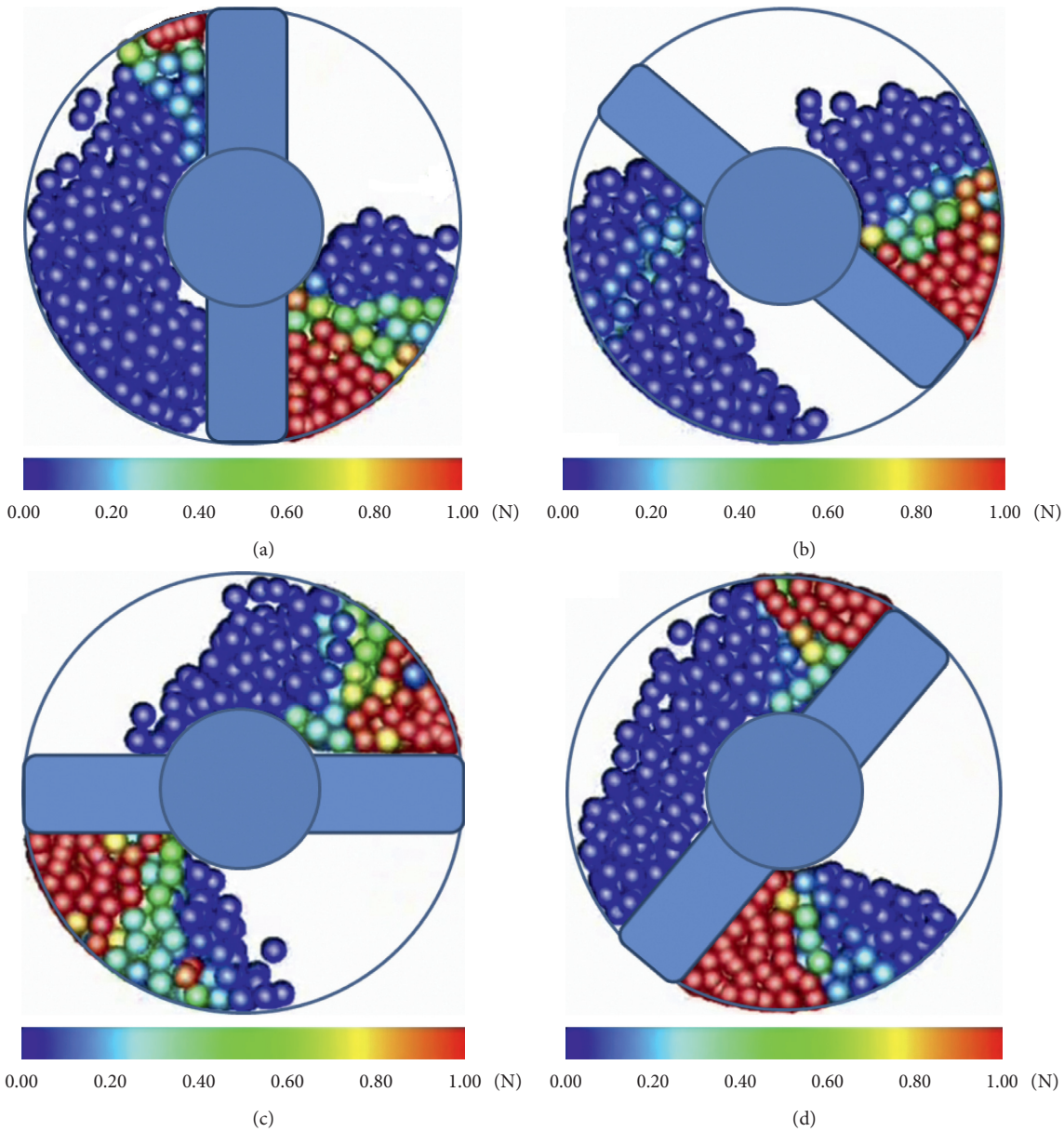

Figure 8: Compressive force acting on the particle inside the rotary damper with the no-gap model; the packing fraction is 50%, and the rotational speed is 60 rpm. (a) 0 degree, (b) 45 degrees, (c) 90 degrees, and (d) 135 degrees. The direction of rotation is counter-clockwise.

mention that the rotary damper with the gap between rotor and cylinder and no gap between rotor and cylinder may look similar, but in the case of the gap model, due to the gap between the damper body and the rotor, an extra layer of elastomer particles is formed. In the gap between rotor and cylinder, particles are under a strongly compressed state, resulting in the generation of a strong friction zone inside the damper.

4.2. Effect of Packing Fraction and Rotor Speed on Damper Torque of the Damper. Packing fraction can be defined as the mass of the particles divided by the volume of the damper and the density of the particles [1]. Rotary elastomer particle damper shows an increase in damper torque with the increase of packing fraction. Figure 10 shows the torque vs. packing fraction graph of no-gap models of rotary elastomer particle dampers. Figure 11 shows the torque vs. packing fraction graph of gap models of rotary elastomer particle dampers. Similar observations are made in gap and no-gap models of rotary elastomer particle dampers; they both showed an increase in damper torque with the increase of packing fraction. The main reason is that the number of particles decreases inside the damper with a decrease in packing fraction [20]. A small variation in particle number leads to a large change in damping behavior. A decrease in the number of particles increases the volume of void gaps in the rotary elastomer particle damper. When elastomer particles are moved forward by the rotor at a high packing fraction, the particles do not have void spaces available.

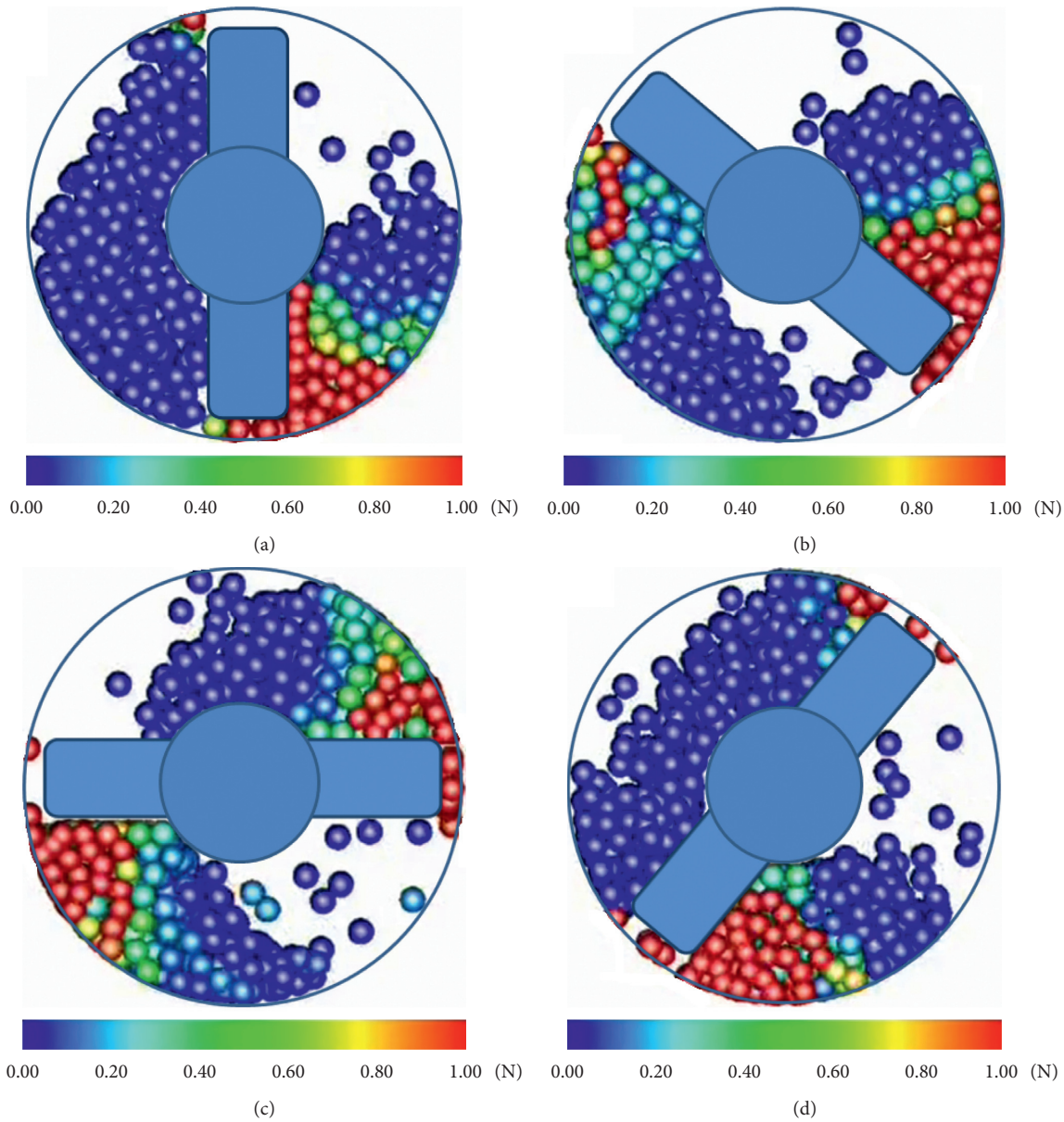

Figure 9: Compressive force acting on the particle inside the rotary damper with the gap model; the packing fraction is 50%, and the rotational speed is 60 rpm. (a) 0 degree, (b) 45 degrees, (c) 90 degrees, and (d) 135 degrees. The direction of rotation is counter-clockwise.

When there are void gaps, particles do not apply strong frictional forces on each other and the walls of the damper [18]. However, when the void gaps are large, the particles are not strongly compressed by neighboring particles, so particles produce weak repulsive forces. The elastic deformation of elastomer particles inside the damper plays a vital role in increasing the damper torque. In short, when there are fewer void gaps inside the damper, particles can produce strong damper torque. As illustrated in Figures 10 and 11, the damper torque increases not only because of the packing fraction but also the rotational speed of the rotor. One of the important factors which cause an increase in damper torque with the increase of rotor speed is the normal and tangential forces acting on the elastomer particles which are strong at high speed of the rotor. The second reason is the increase in the number of collisions between particle-particle and particle-wall. A high-speed rotor pushes the elastomer particles with higher velocity, and particles collide with neighboring particles with high velocity, and loss of energy takes place. In Figure 11, until 10 rpm of the shaft, the damper torque of rotary damper with the gap between rotor and cylinder is higher than the rotary damper with no gap between rotor and cylinder. After 10 rpm of the shaft, the rotary elastomer damper with no-gap model has higher damper torque than the rotary damper with gap model using 3 mm diameter particles. From 1 to 10 rpm, the gap model produced higher damper torque, because at low speed of rotor, particles were crossing the gap region by rolling motion. Due to rolling motion, particles were experiencing compression. At the high rpm of the shaft, the particles

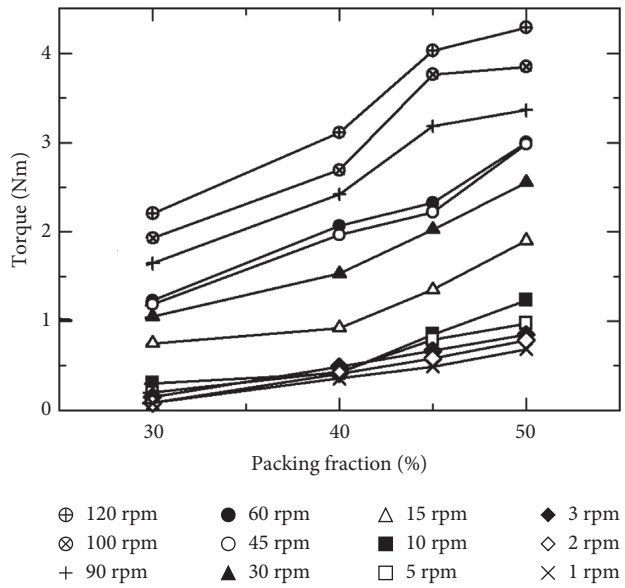

Figure 10: The torque versus packing fraction curve of the rotary damper with no gap between the rotor and cylinder using 3 mm diameter particle made from TSE3466.

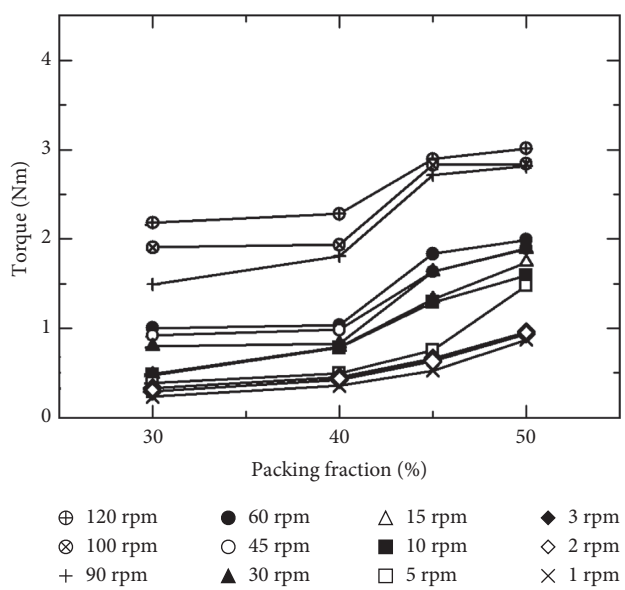

Figure 11: The torque versus packing fraction curve of the rotary damper with gap between the rotor and cylinder using 3 mm diameter particle made from TSE3466.

rolling motion converted to sliding motion when passing through the gap region. In conclusion, due to sliding motion at high rpm, compressive force on particles reduced; that is why after 10 rpm, the no-gap model's damper torque is higher than the rotary damper with gap model.

It is worth mentioning that an increase in packing fraction and the rotational speed increases the damper torque, but it has certain limitations. At high rotational speeds such as 100 and 120 rpm, the particle breaking rate is higher. Similarly, high rpm of the rotor for a long period can also break the particles.

Previous studies showed that, after a certain packing fraction, a decline in the damping is observed in metallic particle dampers, but in the case of elastomer damper until 50% packing fraction, the damper torque kept on increasing. We could not observe the limit of packing fraction after which the damper torque may reduce in rotary elastomer particle damper too, because at high packing fractions such as 70% and above, it is difficult to close the cylinder.

4.3. Effect of Change in Size of Particles on Damper Torque of the Damper. The particles of 3 mm, 4 mm, and 5 mm made from TSE3466 were experimentally tested. This section of the study demonstrates a correlation between the damper torque and the size of elastomer particles. Although the mass ratio is kept constant, the number of particles would vary. In the case of the gap and no-gap models, increase in damper torque was observed with the increase of the size of the elastomer particles. Figure 12 shows the collective results of 3 mm, 4 mm, and 5 mm diameter particles at 60 rpm. It is observed that the size of elastomer particles plays a significant role in increasing the damper torque of a rotary elastomer particle damper. A significant increase in damper torque is obtained when 5 mm diameter elastomer particles are used. The main reason behind the increase in the damper torque with the increase of particle size is the higher deformation capability in large-sized particles. Due to collision and friction between particles and damper body, the velocity of the adjacent particles drops. Particle velocity drops when two particles collide with each other and compares each other. The greater energy dissipation and damping take place when collision and compression are transferred to neighboring particles. Large particles have more contact area and can deform more than small particles under a compressed state. In brief, large size particles tend to produce strong repulsive forces and so result in strong damper torque. It is worth mentioning that when 5 mm diameter particles are used inside the rotary damper with gap mode, it produces higher damper torque than the rotary damper with the no-gap model. When particles of 5 mm diameters entered into the gap, 5 mm particles were under intense compressive force due to larger deformation capability. In summary, unlike 3 mm and 4 mm diameter particles, 5 mm particles are in a strongly compressed state even at high rpm, resulting in a strong damper torque generation.

4.4. Effect of Gap between the Rotor and Cylinder on Damper Torque of the Damper. In order to investigate the effect of the gap between rotor and cylinder, rotary elastomer particle dampers with gap and no gap between rotor and cylinder are used in this paper. Some of the interesting and unique results are obtained from the study. As illustrated in Figure 13, damper torque of rotary damper with gap model using 3 mm diameter particles is higher until the 10 rpm of the shaft. After 10 rpm of the shaft, the decrease in the damper torque of the rotary damper with the gap model compared to the no-gap model is due to the sliding of particles through the gap. At the low rotational speed of the shaft, particles slowly cross from the gap between the rotor and the body of the

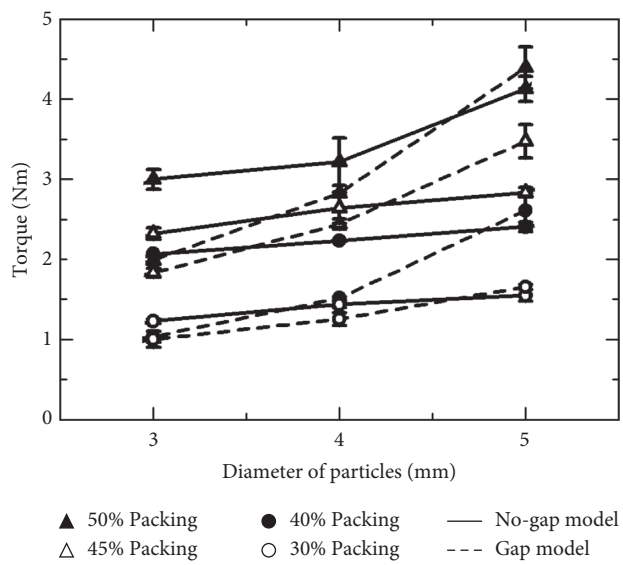

Figure 12: The torque versus diameter of the particle curve of the rotary damper with gap and no-gap models at 60 rpm.

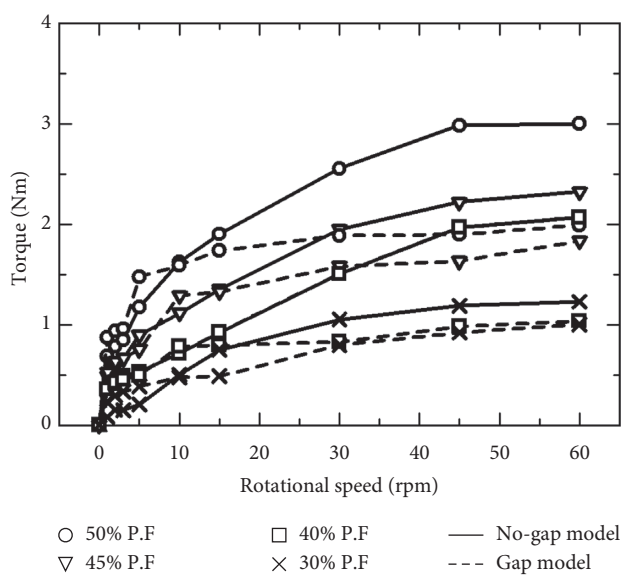

Figure 13: The torque versus rotational speed curve of the rotary damper with gap and no gap using 3 mm diameter elastomer particles.

damper. Due to the rotational motion of particles, strong frictional forces are generated. This rotation of particles turns into a sliding motion when the rotor strongly pushes particles at rpm (more than 10 rpm). In summary, particles do not go through enormous compression at high rpm while crossing through the gap region. At high rpm, they quickly cross the gap region by sliding, which results in weak compressive forces on the particles. However, in the case of the rotary damper with a no-gap model, there is no gap region, but the neighboring particles support particles in front of the rotor. In the gap model, the particles cross from the gap region, so at high rpm, the neighboring particles' support is weak compared to the rotary damper with no gap.

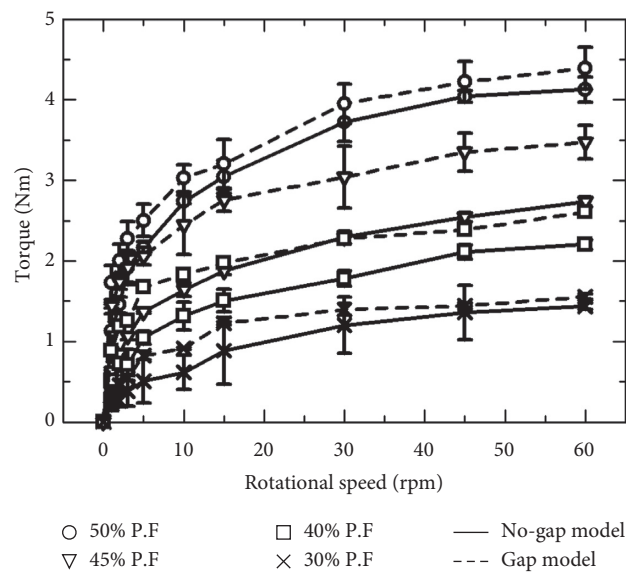

Figure 14: The torque versus rotational speed curve of the rotary damper with gap and no-gap models using 5 mm diameter elastomer particles.

In Figure 14, interesting results are obtained when elastomer particles of 5 mm diameter are used. Interestingly, the damper torque of the rotary damper with the gap model is larger than the rotary damper with the no-gap model when 5 mm diameter particles are used. Because of the higher deformation capability of 5 mm diameter particles compared to 4 mm and 3 mm diameter particles, 5 mm diameter particles have more contact area, and they can deform more under a compressed state. In conclusion, 5 mm diameter elastomer particles tend to produce strong repulsive forces, resulting in strong damper torque. In summary, unlike 3 mm and 4 mm diameter particles, 5 mm particles are in the strongly compressed state even at high rpm, which results in the generation of a strong damper torque.

4.5. Findings and Significance in Comparison to Existing Approaches. In this subsection, we discuss the unique and significant findings of this study by comparing it with the state-of-the-art approaches.

(1) Usually, particle dampers consist of metallic particles, but metallic particles produce enormous noise due to collision between particle-particle and particle-wall [13]. In this study, we used elastomer particles instead of metallic particles. Elastomer particles do not produce noise due to collision between particle-particle and particle-wall because of their soft nature.

(2) Research on metallic particles showed that after a specific diameter of particles, further increase in the size of particles reduced the damping performance [12]. However, we used elastomer particles of 3 mm, 4 mm, and 5 mm diameter; no reduction in damper torque is observed with an increase in the size of elastomer particles.

(3) Generally, in metallic particles, after a specific limit of packing fraction, further increase in the packing fraction reduced the damping capabilities of the damper [9, 10, 12, 16]. However, we used elastomer particles, and no reduction in damper torque is noticed with the increase in the packing fraction.

(4) This study proved that particle deformation plays a significant role in producing higher damping in elastomer particle dampers. The elastomer particles in front of the rotor play a vital role in producing strong damper torque because they have strong compressive forces.

(5) Gap and no gap between the rotor and the cylinder with respect to different sizes of elastomer particles have not been studied in previous studies. In this research, we proved that to obtain higher damping, it is recommended to use a no-gap model when elastomer particles with 3 mm diameter are used inside the damper. However, when the particles size is 5 mm, the damper with the gap between rotor and cylinder can produce higher damping.

5. Conclusion

We investigated the effect of change in packing fraction, rotor speed, size of elastomer particles, and the gap between the rotor and cylinder on the damper torque. Prototypes of the rotary elastomer particle damper with gap and no gap between rotor and cylinder were introduced to observe the damper torque performance of rotary elastomer damper. Spherical elastomer particles made from TSE3466 are tested in the rotary damper with 3 mm, 4 mm, and 5 mm diameters. An increase in damper torque is observed by increasing the packing fraction. Particles made of TSE3466 were tested to observe the effect of the particles' size on damper performance. It is proved that 5 mm diameter particles showed higher damper torque than 4 mm and 3 mm diameter particles. Interestingly, the damper torque of the rotary damper with the gap model was higher than the no-gap model until 10 rpm of the shaft when 3 mm diameter elastomer particles were used. The damper torque of the rotary damper with the gap between rotor and cylinder is larger than the rotary damper with a no-gap model throughout any rpm when 5 mm diameter elastomer particles are used.

Data Availability

The data supporting the findings of this study are available within the article. Further, any specific data will be provided by the corresponding author upon reasonable request.

Consent

This article does not contain any studies with human participants.

Conflicts of Interest

The authors declare that they have no conflicts of interest.

References

[1] R. Kawamoto, Y. Ido, and A. Toyouchi, "Damping properties of a damper using an elastomer particle assemblage containing fine particles," *Advanced Experimental Mechanics*, vol. 1-10, pp. 99–104, 2016.

[2] X. Li, Y. Yang, and W. Shi, "Study on the damping effect of particle dampers considering different surface properties," *Shock and Vibration*, vol. 2019, Article ID 8293654, 16 pages, 2019.

[3] Z. Lu, X. Lu, H. Jiang, and S. F. Masri, "Discrete element method simulation and experimental validation of particle damper system," *Engineering Computations*, vol. 31, no. 4, pp. 810–823, 2014.

[4] Z. Lu, Z. Wang, S. F. Masri, and X. Lu, "Particle impact dampers: past, present, and future," *Structural Control and Health Monitoring*, vol. 25, no. 1, 2018.

[5] H. V. Panossian, "Structural damping enhancement via non-obstructive particle damping technique," *Journal of Vibration and Acoustics*, vol. 114, no. 1, pp. 101–105, 1992.

[6] K. S. Marhadi and V. K. Kinra, "Particle impact damping: effect of mass ratio, material, and shape," *Journal of Sound and Vibration*, vol. 283, no. 1-2, pp. 433–448, 2005.

[7] M. Sánchez, C. M. Carlevaro, and L. A. Pugnaloni, "Effect of particle shape and fragmentation on the response of particle dampers," *Journal of Vibration and Control*, vol. 20, no. 12, pp. 1846–1854, 2013.

[8] W. Liu, G. R. Tomlinson, and J. A. Rongong, "The dynamic characterisation of disk geometry particle dampers," *Journal of Sound and Vibration*, vol. 280, no. 3-5, pp. 849–861, 2005.

[9] A. Papalou and S. F. Masri, "Response of impact dampers with granular materials under random excitation," *Earthquake Engineering & Structural Dynamics*, vol. 25, no. 3, pp. 253–267, 1996.

[10] R. D. Friend and V. K. Kinra, "Particle impact damping," *Journal of Sound and Vibration*, vol. 233, no. 1, pp. 93–118, 2000.

[11] F. Duvigneau, S. Koch, E. Woschke, and U. Gabbert, "An effective vibration reduction concept for automotive applications based on granular-filled cavities," *Journal of Vibration and Control*, vol. 24, no. 1, pp. 73–82, 2018.

[12] P. S. Kachare and K. Bimleshkumar, "Effect of particle size and packing ratio of PID on vibration amplitude of beam," *Journal of Mechanical Engineering and Sciences*, vol. 4, pp. 504–517, 2013.

[13] H. Ye, Y. Wang, B. Liu, and X. Jiang, "Experimental study on the damping effect of multi-unit particle dampers applied to bracket structure," *Applied Sciences*, vol. 9, no. 14, 2019.

[14] Y. Morishita, Y. Ido, K. Maekawa, and A. Toyouchi, "Basic damping property of a double-rod type damper utilizing an elastomer particle assemblage," *Advanced Experimental Mechanics*, vol. 1-21, pp. 93–98, 2016.

[15] K. K. Kishan, Y. Ido, Y. Iwamoto, and A. Toyouchi, "Experimental investigation of angle dependent torque properties of a particle rotary damper using a magnetic elastomer particle assemblage," *International Symposium on Applied Electromagnetics and Mechanics*, vol. 64, pp. 737–743, 2020.

[16] Z. Lu and M. W. Yan, "A survey of particle damping technology," *Zhendong yu Chongji/Journal of Vibration and Shock*, vol. 32-7, pp. 1–7, 2013.

[17] B. Darabi and J. A. Rongong, "Polymeric particle dampers under steady-state vertical vibrations," *Journal of Sound and Vibration*, vol. 331, no. 14, pp. 3304–3316, 2012.

[18] A. Toyouchi, M. Hanai, Y. Ido, and Y. Iwamoto, "Damper force characteristics of a separated dual-chamber single-rod-type damper using an elastomer-particle assemblage," *Journal of Sound and Vibration*, vol. 488, Article ID 115625, 2020.

[19] *The Japan Society of Mechanical Engineers, JSME Mechanical Engineers' Handbook*Maruzen Publishing Co.,Ltd, Tokyo, Japan, 6 edition, pp. 3–34, Tokyo, Japan, 1977, (in Japanese).

[20] K. Alireza and Z. Mansourpour, "Influence of non-spherical shape approximation on DEM simulation accuracy by multi-sphere method," *Powder Technology*, vol. 332, pp. 265–278, 2018.